THESIS FOR THE DEGREE OF DOCTOR OF PHILOSOPHY

Improving Thermoelectric Properties of Inorganic Clathrates by Atomic and Microscale Structure Engineering

Yifei Zhang

Department of Chemistry and Chemical Engineering
CHALMERS UNIVERSITY OF TECHNOLOGY

Göteborg, Sweden 2021

Improving Thermoelectric Properties of Inorganic Clathrates by Atomic and Microscale Structure Engineering

YIFEI ZHANG

ISBN 978-91-7905-575-2

Doktorsavhandlingar vid Chalmers tekniska högskola
Ny serie nr 5042
ISSN 0346-718X

Department of Chemistry and Chemical Engineering
Chalmers University of Technology
SE-412 96 Göteborg
Sweden
Telephone: +46 (0)31-772 1000

From left to right showing the microstructure, atomic structure of inorganic clathrates, and the electron and phonon transport

Printed by Chalmers Reproservice
Gothenburg, Sweden 2021

Improving Thermoelectric Properties of Inorganic Clathrates by Atomic and Microscale Structure Engineering

YIFEI ZHANG
Department of Chemistry and Chemical Engineering
Chalmers University of Technology

Abstract

As more countries are aiming for a carbon-neutral economy, technologies that utilize renewable energies are increasingly being considered. Thermoelectric materials enable the direct conversion between a thermal gradient and an electrical potential gradient, and are thus exploited for applications such as waste heat recovery. One of the prominent thermoelectric materials is the inorganic clathrate. Extensive research has been conducted over the past few decades to utilize its properties. However, several problems still remain ambiguous.

In this thesis, we have studied the atomic and microscale structure of the clathrates and investigated its impact on the thermoelectric properties. Especially, with a combination of experiment and theoretical calculations, the existence of an order-disorder phase transition is confirmed. It further influences the electrical transport properties, since the band structure changes after the phase transition. The degree of chemical ordering can be controlled by the synthesis method, because materials reach different equilibrium states in either route. In addition, it is found that atomic vacancies can induce a peculiar transition effect in the electrical resistivity.

In order to investigate its influence on the thermoelectric performance, a novel method is employed, where $Ba_8(Al_xGa_{1-x})_{16}Ge_{30}$ clathrates are synthesized by alloying $Ba_8Al_{16}Ge_{30}$ with $Ba_8Ga_{16}Ge_{30}$. This way a heterostructure is created, which contains the quaternary clathrate main phase and aggregates of Al particles. Consequently, the charge carrier mobility is largely improved to a value higher than that of the single crystal, while the lattice thermal conductivity is reduced due to the enhanced phonon scattering at different length scales.

A greatly improved understanding of the process-structure-property relationship of clathrates is achieved in this thesis. The methodologies used, as well as the key findings, can be applicable for other material systems, and hence facilitate the future research in the thermoelectrics field.

Keywords: Thermoelectrics, Clathrates, Microstructure, Crystal structure, Chemical ordering, Electrical transport properties, Thermal properties

List of Publications

I. Enhanced Thermoelectric Performance of $Ba_8Ga_{16}Ge_{30}$ Clathrate by Modulation Doping and Improved Carrier Mobility.
Yifei Zhang, Joakim Brorsson, Ren Qiu, Anders E. C. Palmqvist
Advanced Electronic Materials, 2021, 7(2), 2000782

II. Order-Disorder Transition in Inorganic Clathrates Controls Electrical Transport Properties.
Joakim Brorsson, **Yifei Zhang**, Anders E. C. Palmqvist, Paul Erhart
Chemistry of Materials 2021, 33 (12), 4500-4509

III. Investigating the Chemical Ordering in Quaternary Clathrate $Ba_8Al_xGa_{16-x}Ge_{30}$.
Yifei Zhang, Joakim Brorsson, Takashi Kamiyama, Takashi Saito, Paul Erhart, Anders E. C. Palmqvist
Accepted by Inorganic Chemistry

IV. Effect of Al/Ga Ratio on Atomic Vacancies Content and Thermoelectric Properties in $Ba_8Al_xGa_{16-x}Ge_{30}$Clathrates.
Yifei Zhang, Joakim Brorsson, Ren Qiu, Paul Erhart, Anders E. C. Palmqvist
Manuscript

V. Effect of Ce Doping on the Thermoelectric Properties of $Ba_8Al_xGa_{16-x}Ge_{30}$Clathrates.
Yifei Zhang, Anders E. C. Palmqvist
Manuscript

Contribution Report

I. Lead author. Performed all the experiments, analyzed the results and wrote the manuscript.

II. Participated in the synthesis of materials, measured the specific heat capacity and electrical transport properties, analyzed the results and jointly wrote the manuscript.

III. Lead author. Except the theoretical calculations, performed all the experiments, analyzed the results and wrote the manuscript.

IV. Lead author. Except the theoretical calculations, performed all the experiments, analyzed the results and wrote the manuscript.

V. Lead author. Performed all the experiments, analyzed the results and wrote the manuscript.

List of Physical Properties and Abbreviations

B quality factor.

F_{hkl} structure factor.

PF power factor.

S Seebeck coefficient.

κ thermal conductivity.

κ_e electronic thermal conductivity.

κ_l lattice thermal conductivity.

μ charge carrier mobility.

μ_w weighted charge carrier mobility.

ρ electrical resistivity.

σ electrical conductivity.

c_p specific heat capacity.

k_B Boltzmann constant.

m^* effective mass.

n carrier concentration.

zT figure of merit.

ADP atomic displacement parameter.

APS acoustic phonon scattering.

DOS density of states.

DSC differential scanning calorimetry.

EDX energy-dispersive X-ray fluorescence analysis.

IIS ionized impurity scattering.

PGEC phonon-glass electron-crystal.

SEM scanning electron microscopy.

SOF site occupation factor.

SPS spark plasma sintering.

TCR temperature coefficient of resistivity.

WDX wavelength-dispersive X-ray fluorescence analysis.

XRD X-ray diffraction.

XRF X-ray fluorescence analysis.

Contents

1 Introduction

1.1 Background

The 21st Century will become the most important and most challenging century in human history. EU, China and US are all aiming to be carbon-neutral by 2050, an economy with net-zero greenhouse gas emission. The economic, political and environmental demands have driven the society and research to the technologies that can utilize renewable energy, *i.e.*, energy-conversion applications. One of these technologies is based on thermoelectric materials, which can convert waste heat into electricity. According to the International Energy Agency, in 2018 the total utilized energy was only 32 % in US, while 68 % of energy was wasted in the form of heat.[1] Especially, approximately 6000 GWh waste heat was generated, mainly in the steel-making plants and oil refineries. It is therefore of great interest to implement with thermoelectric devices in the heavy industry, in order to reduce CO_2 emission and to provide improved energy utilization.[2]

The state-of-the-art thermoelectric materials can be categorized according to the working temperature: Bi_2Te_3-based around room temperature ($<$ 100 °C), PbTe-based for medium temperature (300 - 600 °C) and SiGe-based at high temperature ($>$ 600 °C).[3–7] The room-temperature devices are mainly for active cooling and commercial applications are available for temperature management solutions for automotive, medical, electronics and batteries, using solid-state thermoelectric materials. The discovery and development of organic thermoelectric materials have led to more possibilities for room-temperature applications, such as wearable and flexible electronics that use a temperature difference of only few degrees between human skin and air.[8] High-temperature thermoelectric applications refer to Radioisotope Thermoelectric Generators (RTGs), and have long been used as the only power source in satellites and space probes.[8] RTGs have proved its reliability and robustness for deep-space exploration, especially, even after 23 years, the power output of spacecraft Voyager still remained 80 % of its initial design.[9]

The medium-temperature application is most economically interesting, since large amount of waste heat is within this temperature range. However, unlike other thermoelectric applications which have already found their unique market share or provide the exclusive energy conversion choice, the medium-temperature

application is not totally commercialized, mainly because of the low efficiency.[8] As shown in Figure 1.1, compared to the solar cell, the current efficiency of thermoelectric conversion is low. Even though the thermoelectric figure of merit zT is improved from 2 to 3 (50 % improvement for the thermoelectric performance), the efficiency is still not compelling. It should also be noted that there are only a few cases that have reached this performance in lab. In addition, the state-of-the-art medium-temperature material PbTe contains toxic (Pb) and scarce (Te) elements, which further hinders mass production. Improving the thermoelectric efficiency, as well as finding materials containing non-toxic and abundant elements, is the future for thermoelectrics.[10]

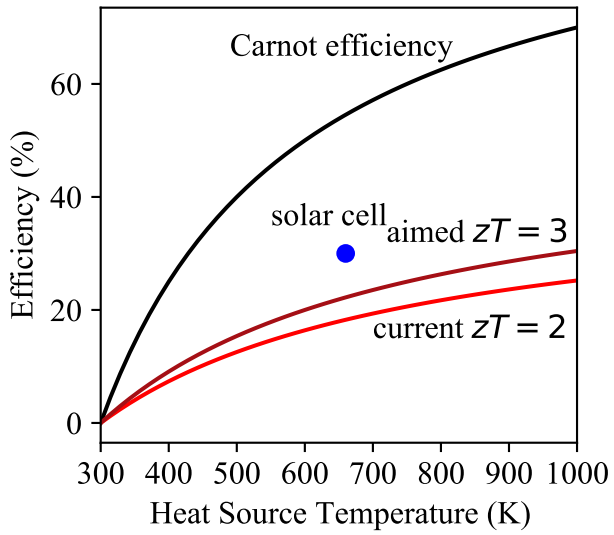

Figure 1.1: *Efficiency of thermoelectric conversion (current status and future goal is indicated by the light and dark red lines, respectively), in comparison with Carnot efficiency and efficiency of solar cell.*

One of the prominent thermoelectric materials is the inorganic clathrate.[3] They are semiconductor materials exhibiting unique crystal structure, with nanosized cages that contain guest atoms, ions or molecules. On the other hand, clathrates possess intrinsically low thermal conductivity, which is close to the amorphous limit. The combination of the semiconductor nature and intrinsically low thermal conductivity, makes clathrates especially interesting for the thermoelectric research.[11–14]

Type-I clathrate is by far the most investigated subgroup, which has been studied for decades. It contains 54 atoms in the unit cell, and extensive research is focusing on tuning the chemical composition, including the alkali-metal-based, alkaline-metal-based, lanthanide-containing, transition-metal-based, semiconducting-element-based (group III, IV and V), and the inverse clathrates. However, none of these shows better thermoelectric

performance than the state-of-the-art clathrate compound $Ba_8Ga_{16}Ge_{30}$. In addition, some issues still remain ambiguous, *e.g.*, thermal stability and the inconsistency in the reported thermoelectric properties. Therefore, a comprehensive understanding of the structure and composition is still lacking.

1.2 Objective of this thesis

The objective of this thesis is to improve the thermoelectric performance of inorganic clathrates, understand the effect of defects (atomic vacancies, dopants, substitution, precipitates) on the electron and phonon transport, and how to control these defects experimentally.

Paper II-V focus on the atomic structure, including the chemical ordering over the host structure, Ce-doping on the guest sites and atomic vacancies. Especially, we have confirmed the order-disorder phase transition, which can explain the inconsistency in the thermoelectric properties and peculiar transition effect. In **Paper I**, we have explored a novel method to engineer the microstructure, in order to improve electron transport and simultaneously reduce phonon transport.

2 Thermoelectrics

2.1 Thermoelectric effect

Thermoelectric effect compromises three effects – Seebeck effect, Peltier effect and Thomson effect, and enables the direct conversion between a temperature gradient and electrical voltage.[15]

In 1822, German physicist Thomas Johann Seebeck discovered that a circuit made from two dissimilar metals with junctions at different temperatures would induce electric current. This phenomenon was later named as Seebeck effect, which describes the ability of converting a temperature difference into electricity. Thermoelectric power generator is thus invented by utilizing the Seebeck effect. As shown in Figure 2.1, this energy-conversion device consists of both n- and p-type semiconductors, which are connected electrically in series and thermally in parallel. When one side of the device is applied with a heat source, the charge carriers (electrons in the n-type and holes in the p-type semiconductors) move along the temperature gradient from the hot side to the cold side, as a result, electric current is generated.

Conversely, electricity can also create a thermal gradient on purpose, which is called Peltier effect. It can be used for thermoelectric refrigeration, to achieve active cooling. Thomson effect is less known, but it relates the two other effects, and concludes that both are characterized by one key property, Seebeck coefficient (S).

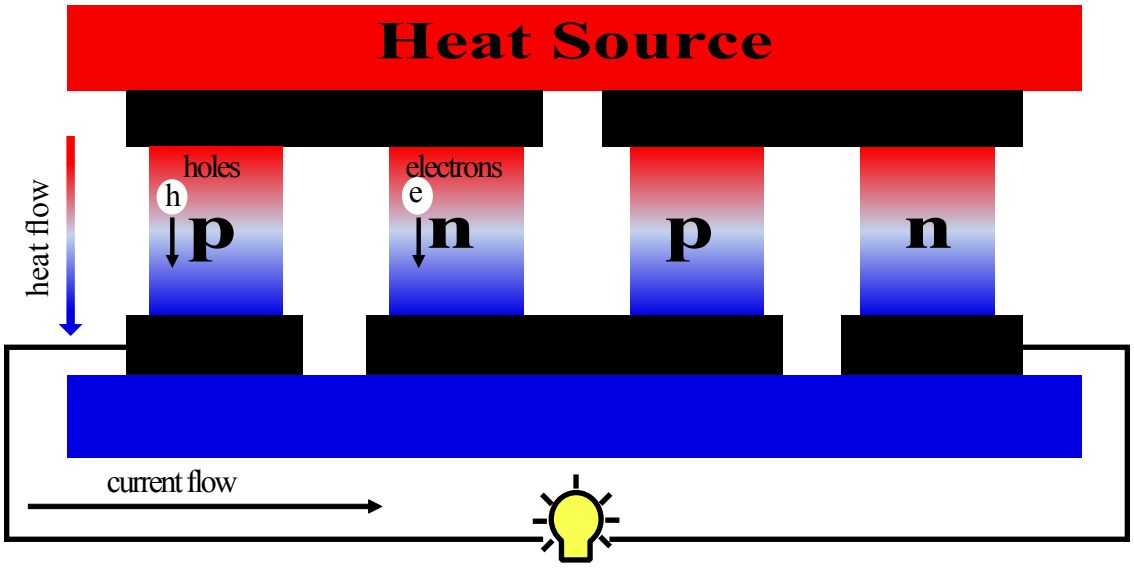

Figure 2.1: *Illustration of thermoelectric power generator, which includes both n- and p-type semiconductor materials. Electricity is generated via Seebeck effect when the top side of the generator is close to a heat source.*

2.2 Thermoelectric properties

2.2.1 Thermoelectric efficiency and figure of merit

The efficiency of thermoelectric conversion (η) is defined by Equation 2.1.

$$\eta = \frac{T_h - T_c}{T_h} \cdot \frac{\sqrt{1+zT}-1}{\sqrt{1+zT}+\frac{T_c}{T_h}} \tag{2.1}$$

Here T_h and T_c refer to the temperature on the hot side and the cold side of the device, respectively. Therefore, to increase the conversion efficiency, in other words, is to improve zT.

zT is the so-called thermoelectric figure of merit, which describes the intrinsic thermoelectric performance of a material:

$$zT = \frac{S^2 \cdot \sigma}{\kappa} \cdot T \tag{2.2}$$

and includes three material parameters: Seebeck coefficient (S) measures the ability of the coupling between temperature gradient and potential gradient; σ and κ refer to the electrical and thermal conductivity, respectively.

2.2.2 Seebeck coefficient

Seebeck coefficient is the ratio between a thermoelectric voltage and the corresponding temperature gradient across the material, as shown in Equation 2.3. It shows negative value for n-type semiconductors and positive for the p-type.

$$S = -\frac{\triangle V}{\triangle T} \tag{2.3}$$

High absolute value of Seebeck coefficient is the prerequisite for thermoelectric materials, typically the maximum value should be higher than 200 µV/K. Nevertheless, improving Seebeck coefficient is not straightforward. Seebeck coefficient can be expressed as:[16]

$$S = \frac{\pi^2}{3}\frac{k_B}{e}(k_B T)\left[\frac{1}{n(E)}\frac{dn(E)}{dE} + \frac{1}{\mu(E)}\frac{d\mu(E)}{dE}\right]_{E_F} \tag{2.4}$$

Here, k_B is the Boltzmannn constant, $n(E)$ and $\mu(E)$ refer to the density of states and charge carrier mobility, respectively. E is the energy level in the band structure, and E_F refers to the Fermi level specifically.

Clearly, S depends on two different terms:

1. $\frac{1}{n(E)}\frac{dn(E)}{dE}$, which is related to the density of states near Fermi level;

2. $\frac{1}{\mu(E)}\frac{d\mu(E)}{dE}$, which is related to the charge carrier mobility.

Therefore, Seebeck coefficient can be maximized by a sharp change in the band structure near the Fermi level, which can be achieved through resonant states and band convergence.[17, 18] Alternatively, one can optimize the charge carrier mobility (μ) by tuning the charge carrier scattering mechanism.

2.2.3 Electrical resistivity

Electrical resistivity (ρ) and conductivity (σ) are determined by the charge carrier concentration (n) and charge carrier mobility (μ):

$$\sigma = 1/\rho = ne\mu \tag{2.5}$$

Doping is the most common way to tune the charge carrier concentration. The charge carrier mobility is mainly influenced by the scattering mechanism of the charge carrier, including acoustic phonon scattering (APS)[19], ionized impurity scattering (IIS)[20–22] and alloy scattering.[23]

2.2.4 Thermal conductivity

Thermal conductivity is the ability of a material to conduct heat. Typically in solid materials, it comprises electronic thermal conductivity (κ_e) and lattice thermal conductivity (κ_l):

$$\kappa = \kappa_e + \kappa_l \tag{2.6}$$

The former term κ_e can be evaluated from the electrical conductivity (σ) by Wiedemann-Franz law with Lorentz number L:

$$\kappa_e = LT\sigma \tag{2.7}$$

Lattice thermal conductivity (κ_l) cannot be measured directly, instead, it is usually obtained by subtracting the electronic contribution from the total thermal conductivity. Low κ_l is important, and especially semiconductor materials with large anharmonicity and complex crystal structure are always good candidates for thermoelectric applications.[13] Also, one can enhance the phonon scattering and reduce the phonon mean free path, which can be done by introducing defects, such as dislocations and nanoparticles/nanoinclusions.[24]

2.3 Strategies to improve thermoelectric performance

To improve the thermoelectric performance, according to Equation 2.2, Seebeck coefficient and electrical conductivity should be maximized, meanwhile the thermal conductivity should be suppressed as much as possible. However, due to the interconnection between these physical properties, all three parameters cannot be improved simultaneously. It is already a significant breakthrough to enhance one parameter without counteracting others.

Electrical conductivity can be boosted by doping as the carrier concentration is increased, but a too high carrier concentration is unfavorable for the Seebeck coefficient, and the increase of the electrical conductivity inevitably leads to a higher electronic thermal conductivity. As shown in Figure 2.2, optimal zT lies between the carrier concentration from $10^{19}\,\mathrm{cm}^{-3}$ to $10^{20}\,\mathrm{cm}^{-3}$.[3]

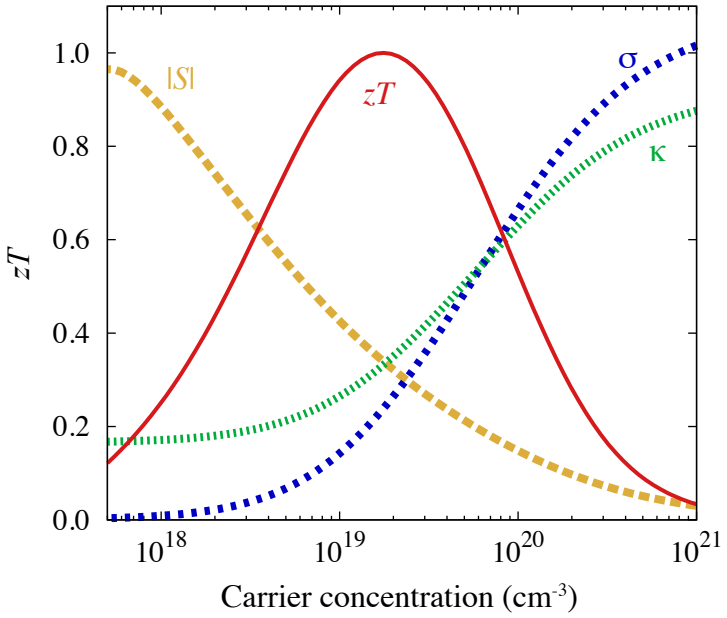

Figure 2.2: *Carrier concentration dependence of S, σ, κ and zT.*

Nanotechnology has boosted the thermoelectric performance over the past few decades, by reducing the lattice thermal conductivity through the introduction of nanoparticles, nanoinclusions and defects.[24] However, a reduction in charge carrier mobility is always observed as well. Without the fundamental understanding and appropriate selection of the materials, nanotechnology could even worsen the overall thermoelectric performance.

Therefore, in order to optimize these three macroscopic measurable parameters (S, σ, κ), the understanding of the microscopic structure and electron/phonon transport mechanism is needed. Herein, we summarize the strategies that are used to improve the thermoelectric performance in this thesis.

2.3.1 Intrinsic materials property – quality factor

Development of thermoelectric materials involves time-consuming trials and errors, it is thus critical to know if a specific material is worth investigating and to which extent the material can be optimized. Thermoelectric quality factor (B) describes the intrinsic microscopic band structure and electron/phonon transport parameters: [10]

$$B \propto \frac{\mu \cdot m^{*1.5} \cdot T^{2.5}}{\kappa_l} \tag{2.8}$$

Here, m^* is the effective mass. As can be seen in Equation 2.8, B shows the importance of decoupling between μ and m^* and meanwhile minimizing κ_l. In addition, as B is no longer dependent on the carrier concentration, it is a

useful indicator during the practical research for estimating the thermoelectric performance. Similarly, there is also electronic quality factor that evaluates power factor ($PF = S^2\sigma$) solely.[25]

Based on B, phonon-glass electron-crystal concept (PGEC) was proposed,[15] suggesting that materials with low κ_l (glass-like thermal conductivity) and high σ (crystal-like electrical conductivity) are ideal thermoelectric materials. Glasses and amorphous materials, having no periodic arrangement of atoms, in general exhibit the lowest thermal conductivity. On the other hand, crystalline materials show excellent electrical conductivity because they preserve well-defined structure.

Skutterudite and clathrate compounds are the first to combine such contradictory properties.[26, 27] They possess cage-like framework structure, where guest atoms are encapsulated inside. These guest atoms are loosely bonded, as their radius is much smaller than the cage size.[28] Therefore, the guest atoms vibrate with large amplitude and scatter phonons, leading to a glass-like κ_l. On the other hand, μ remains large enough, as the electrons transport via the bonding between the atoms of the host framework, so good electrical conductivity is still maintained.[29]

As PGEC concept mainly focuses on the electron/phonon transport properties, recent development in thermoelectrics also involves the band structure (m^*). [10, 16] High-symmetry crystal structure evokes high band degeneracy, so that enhances density of states (DOS) near Fermi level. Complicated phase transition at elevated temperature also contributes to the DOS. Current promising materials, such as GeTe, Mg_3Sb_2, SnSe, Cu_2Se, all possess such features. [30–34]

2.3.2 Electron transport

Electrons (or holes in p-type semiconductor) moving in solid-state materials are scattered by defects, and the charge carrier mobility is thus reduced. Improving the electron transport, in other words, is to improve the charge carrier mobility μ. This can be done, for example, by introducing defects or improving the interfaces.

Early studies primarily focus on the introduction of atomic defects, such as dopants, substitution, solid solution/alloy, which can affect the charge carrier mobility by altering the electron scattering mechanism. At elevated temperature, electrons are scattered by the thermal activated acoustic phonons, so the acoustic phonon scattering (APS) is the dominant scattering mechanism for most thermoelectric materials,[19] resulting in the charge carrier mobility $\mu \propto T^{-3/2}$. If the atoms are randomly substituted by the isovalent atoms, alloy scattering should also be taken into account[35, 36], which leads to $\mu \propto T^{-1/2}$. On the other hand, if the lattice contains dopants and/or atomic vacancies, these will, not only change the charge carrier concentration, but also cause locally unbalanced charge. Therefore, the ionized impurity scattering (IIS) appears, whose temperature dependence is $\mu \propto T^{3/2}$. It is noteworthy that even though

the atomic vacancies can scatter phonon and thus reduce the lattice thermal conductivity, they are, in general, detrimental because the materials can become thermally unstable. Therefore, large effort has been paid to suppress the vacancy content in the materials, not only in clathrates[37], but also in the newly discovered thermoelectric materials Mg_3Sb_2 and GeTe. [38, 39]

Recent studies have turned to the investigation of interfaces and grain boundaries, one of the reasons is that producing polycrystalline materials is more industry-preferable than synthesizing single crystals. Usually nanostructuring in bulk materials increases electron and phonon scattering simultaneously, thus impeding the electron transport. With careful selection of the defects, such as endotaxial nanocrystals,[40] one is able to maintain the charge carrier mobility and meanwhile largely reduce the lattice thermal conductivity. Modulation doping, which creates a heterostructure containing an undoped main phase and dopant precipitates, can even enhance the charge carrier mobility.[41] Investigation of the grain boundary scattering brings more insights.[42] Especially, the concept of grain boundary resistivity is taken into account, and this resistivity can be reduced, *e.g.*, by creating a metallic thin layer on the interfaces. [43]

2.3.3 Phonon transport

Intrinsically low lattice thermal conductivity is the key for thermoelectric materials. The state-of-the-art material PbTe, inorganic clathrate $Ba_8Ga_{16}Ge_{30}$ and newly discovered SnSe, all have an extremely low lattice thermal conductivity, which is close to the glass limit. These materials either possess strong anharmonicity and coupling between the vibrational modes of the phonons, or have complex unit cell and structural disorder.[31, 44, 45]

In order to reduce the lattice thermal conductivity, one can introduce defects in different length scale, which can scatter phonons at various frequencies. [24] This is another reason why recent research has turned to polycrystalline materials rather than the single crystal. However, introducing defects does not necessarily reduce the thermal conductivity, an comprehensive understanding is still needed. Specially, a study on polycrystalline SnSe has brought zT to a record high value, roughly 3.1 at 783 K.[46] The lattice thermal conductivity of the polycrystalline SnSe is significantly lower than that of the single crystal, resulting from the elimination of SnO_x in the interfaces, whose thermal conductivity is much higher than that of SnSe.

2.4 Inorganic clathrates

2.4.1 Atomic structure – host-guest cage compound

Inorganic clathrates are host-guest compounds where the host elements, typically from the group 13 and 14 in the period table, are covalently bonded and form cages which encapsulate the guest atoms, ions and even molecules. [14] Clathrates are classified according to the symmetry, which determines the size and structure of the cages. The most well studied clathrate for thermoelectrics is the type-I, with the space group $Pm\bar{3}n$ (International Tables of Crystallography number 223). Its general composition is $Z_8A_{16}B_{30}$, here Z is the guest atom, while A and B refer to the host elements.

The crystal structure of type-I clathrate is illustrated in Figure 2.3, two cages with different sizes are explicitly shown: small pentagonal dodecahedral and large tetrakaidecahedral cages. Guest atoms are located at the center of the cages, occupying $2a$ and $6d$ Wyckoff sites(large blue and red balls), respectively. Host atoms, as mentioned above, form covalent bonds with each other and share Wyckoff sites $6c$, $16i$ and $24k$ (small red, blue and yellow balls). It should be noted that, the chemical ordering in the host framework is partially ordered: the trivalent element (A in $Z_8A_{16}B_{30}$) preferably occupies the $6c$ site. The reason is that the direct bonding between trivalent elements is energetically unfavorable, and the $6c$ site, as shown in Figure 2.3, is the only position that does not form chemical bond directly with itself.[47, 48]

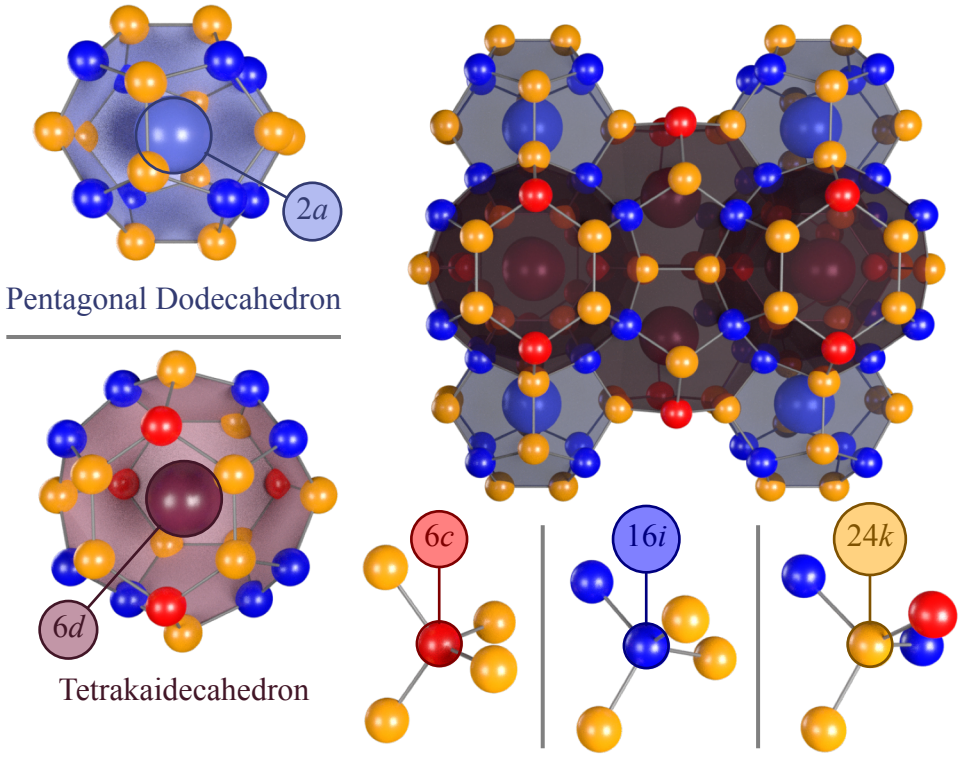

Figure 2.3: *Crystal structure of type-I clathrate (space group $Pm\bar{3}n$). Chemical bonding between host atoms is illustrated in the lower right of the figure.*

Due to the interaction between the guest atoms and cage-like structure, type-I clathrate has intrinsically low thermal conductivity. [13, 45, 47, 49] The phonon vibrational mode of the guest atoms at the 6*d* site (large red balls), interact with the phonons of the host atoms, thus leading to a lower group velocity.[45] As a result, even though clathrate exhibits a crystalline structure, the lattice thermal conductivity is close to the amorphous limit. However, the actual mechanism that induces the glass-like lattice thermal conductivity is still under debate. As the guest atom at the 6*d* site is encapsulated inside an oversized cage, they are loosely bonded and show large atomic vibration, and thus can enhance the phonon scattering. Therefore, the complex host-guest structure of clathrates makes it fascinating for the thermoelectric application, and is also intriguing for the fundamental study.

2.4.2 Zintl concept

Type-I clathrate is characterized as Zintl phase.[11] The guest atoms donate their valence electrons to the bonding among host atoms, and do not participate in bonding directly. In a typical type-I clathrate compound, $Ba_8Ga_{16}Ge_{30}$, the total number of electrons donated by the Ba atoms (nominally +2) is balanced by that of Ga (nominally -1) needed for tetravalent bonding configurations of all

host elements in the unit cell. Thus, the material should behave as an intrinsic semiconductor, and most clathrate compounds are designed based on the Zintl concept. [50]

However, in practice, the synthesized samples usually contain defects such as vacancies, and the real composition deviates from the stoichiometry. If Ga is in excess, the sample shows p-type behavior, conversely if Ge is more than 30 atoms per unit cell, an n-type semiconductor can be obtained. Even with the same nominal composition, the thermoelectric properties of clathrates may differ between samples. This can be due to the chemical ordering, which is known to affect the band structure [51–54].

3 Experimental Methods

3.1 Synthesis methods

3.1.1 Stoichiometric reaction

Stoichiometric reaction is the most straightforward synthesis method for the growth of crystals. All elements are mixed in a crucible, with the mixing ratio being identical to the stoichiometric composition of the intended material. Sample is transferred to a furnace, then heated to a temperature above the melting points of all the elements, and finally cooled to room temperature.

Regarding the synthesis of clathrate compounds $Ba_8Al_xGa_{16-x}Ge_{30}$ in this thesis, due to its high vapor pressure Ba can easily evaporate at elevated temperature. Therefore, additional amount of Ba needs to be added initially, the starting mixing ratio is indeed $Ba_{8.2}Al_xGa_{16-x}Ge_{30}$ rather than $Ba_8Al_xGa_{16-x}Ge_{30}$.

3.1.2 Flux growth

Crystals can also be grown in a 'solvent', here this solvent is called 'flux' and the corresponding method is called flux growth. The flux can be an additional compound apart from the reactants, but can also be one of the reacting elements. In the synthesis of $Ba_8Al_xGa_{16-x}Ge_{30}$, elemental Ga served as flux, because it has the lowest melting point (30 °C) and also the obtained crystals can be easily separated from Ga.

The mixing ratio has a significant impact on the size and quality of the obtained crystals. In previous studies, $Ba_8Ga_{16}Ge_{30}$ was synthesized at the mixing ratio Ba:Ga:Ge=8:64:30, the obtained crystals are single crystals with 10 mm in length.[47] As Ga is in excess, the obtained single crystal shows p-type semiconductor behavior with positive Seebeck coefficient. However, the thermal stability of these crystals is poor, one can observe liquid Ga after heat treatment, and the electrical transport properties change drastically as well.[55]

In **Paper IV**, the mixing ratio has been changed to Ba:Ga:Ge=8:28:30, and the obtained crystals are much smaller, only 3 mm in length. Ga is still in excess but less so, these crystals are sintered to pellets and they all show n-type behavior. It is further revealed that the content of atomic vacancies is closely related to the mixing ratio, and thus affecting the thermal stability of the materials.

3.2 Spark plasma sintering

A dense bulk material with certain dimension is required, when measuring the thermoelectric properties by various instruments. Therefore, the as-synthesized crystals need to be consolidated, and this is done by spark plasma sintering (SPS).

As shown in Figure 3.1, the powder sample is placed inside a punch-die setup and the instrument chamber is in vacuum. As the sintering starts, electric current goes through the setup so the sample is heated by the Joule heating, meanwhile an uniaxial pressure is applied.[56] The sample can be sintered to a dense material within minutes, which is the advantage of SPS over other sintering techniques. However, it is well known that temperature distribution within the sample is not homogeneous, so the sample might not be homogeneous after sintering. Moreover, the temperature that the instrument shows is the temperature at the thermocouple, which is several centimeters away from the sample, so the actual temperature at the sample can be very different and even hundreds of degrees Celsius higher.

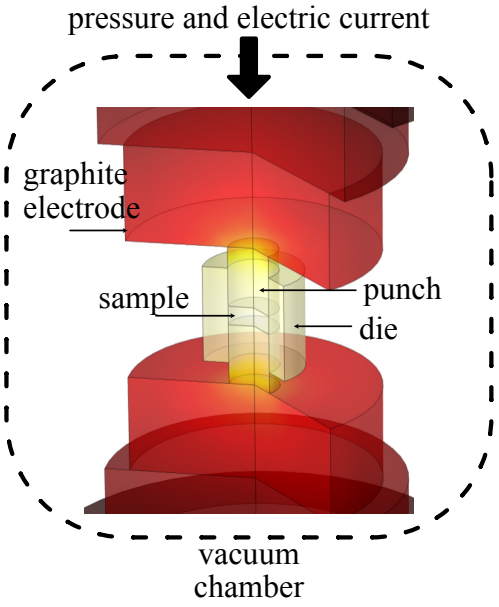

Figure 3.1: *Schematic of SPS setup.*

In order to obtain a dense ($>$ 95 % of theoretical density) pellet, several experimental parameters need to be determined for SPS, among them the most important ones are the sintering temperature, pressure and particle size. It is a time-consuming procedure to find suitable parameters, especially when sintering complex thermoelectric materials and systematic evaluation of experimental trials is necessary. Here is a summary of author's experience of synthesizing $Ba_8Al_xGa_{16-x}Ge_{30}$ clathrates:

1. The inner diameter of our SPS die is 20.5 mm, the desired thickness of the pellet is 2.5 - 6 mm, so the weight for each batch is 3 - 10 g. The sintered sample might not be homogeneous if larger amount of sample is sintered.

2. The particle size distribution should be narrow and within 30 - 60 µm.

3. Two-stage sintering is always used. First stage is heating to 700 °C with 4 min, and holding for 1 min. Second stage is heating to 750 - 820 °C within 1 min, and holding for 15 - 30 min.

4. Fast densification process is important during the sintering, and one can estimate it from the displacement parameter of the SPS instrument. Usually, it should happen at the first stage around 580 - 650 °C, when the sample shrinks approximately 1 mm within 1 min. If it happens at the second stage, one should be careful that the shrinkage should not be too large (> 2 mm), otherwise it means the temperature is too high so the materials are partially melting.

5. Even though the temperature of the second stage is below the melting point of the clathrate, the sample may be melting, so the sintering temperature is the most critical parameter. A long holding time is beneficial for a homogeneous sample.

6. Pressure is always preset to 75 MPa, but one can increase slowly during the sintering. Never increase above 100 MPa, because the graphite punch-die setup can crack.

4 Analytical Techniques

4.1 Structure characterization

4.1.1 X-ray diffraction

X-ray diffraction (XRD) is one of the most important techniques in inorganic chemistry, as it can be used for phase identification, crystal structure determination, and strain and texture analysis.

Bragg's law is the basis of the XRD. As shown in Figure 4.1, crystalline material is a periodic arrangement of atoms (blue dots in the figure). When crystals are bombarded with X-ray beam, only those incident beams satisfying certain criteria can be diffracted constructively in phase. This rule is called Bragg's law:

$$2d_{hkl} \cdot sin\theta = n\lambda \tag{4.1}$$

Here, n can be any integer, λ is the wavelength of the X-ray beam and d_{hkl} refers to the interplanar distance. The diffracted X-ray beam, which is also called reflection, will then be detected by the detector. Therefore, by rotating the angle between the incident beam and the crystal (θ), all the diffracted angles can be detected. Based on the Bragg's law, the corresponding interplanar distances d_{hkl} are known, thus, the space group and the lattice parameter of the crystal can be determined.

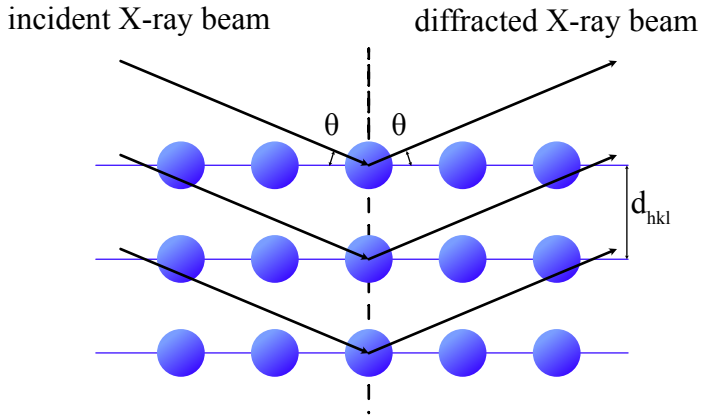

Figure 4.1: *Illustration of Bragg's law. Blue dots represent the periodic arrangement of atoms in a crystal, and blue lines are the atomic planes with Miller indices (hkl) and interplanar distance d_{hkl}. When the crystal is bombarded with X-ray beam, only those incident beams satisfying the Bragg's law can be diffracted constructively in phase..*

The crystal structure is, however, not determined yet, because the atoms on each lattice point is still unknown. The intensity of each reflection (I_{hkl}) needs to be analyzed, as it is proportional to the square of the structure factor (F_{hkl}):

$$I_{hkl} \propto F_{hkl}^2 = osf \cdot \sum_{j=1}^{N} f_j \cdot e^{2\pi \cdot (hx_j + ky_j + lz_j)} \cdot T_j \cdot occ_j \tag{4.2}$$

Here, osf is the scale factor and f_j is the atomic form factor of the element, while x_j, y_j, z_j refer to the position of the atom. T_j is the temperature factor indicating the thermal vibration of the atom. If the atom position is occupied by multiple elements, occ_j refers to the site occupancy factor of each element. Therefore, by resolving the intensity of each reflection, the crystal structure is determined and one can further study the chemical ordering, thermal vibration of the atoms and other crystallographic information.

Nevertheless, instead of solving the intensity of each reflection directly, the crystal structure is determined in the opposite way and the process is called 'refinement': a 'superficial' crystal structure is created and the elements, atomic positions and all structure parameters in Equation 4.2 are 'assumed' initially, the structure factor (F_{hkl}) of this simulated crystal structure is then compared with the experimentally observed value; least squares method is used and the simulated structure is improved by minimizing the difference between the calculated and observed values; until reasonable goodness-of-fit parameters are achieved, at this point, the simulated crystal structure can represent the actual atomic structure of the crystal.

Simple structure can be determined by powder XRD, however, single crystal diffraction is conventionally used for solving complex materials, such as inorganic clathrates. Unlike powder diffraction, single crystal diffraction captures all the individual reflections. Another advantage of single crystal diffraction, is the wider d-spacing (able to determine smaller d_{hkl}) and higher signal-to-noise ratio.

4.1.2 Neutron diffraction

X-ray diffraction always has the 'neighboring element-problem' for those elements with close to similar atomic numbers. In addition, X-ray diffraction is not well-suited for studies of light elements, with small electron clouds, such as H and Li. However, neutron diffraction does not encounter such problems, therefore it is a supplement to XRD. In this thesis, we have used neutron diffraction to study the chemical ordering of Ga and Ge in inorganic clathrates. For X-ray, the scattering cross section is 30.9763 and 31.9774 for Ga and Ge, respectively, less than 3.2 % in difference. In contrast, the neutron scattering length is 7.288 and 8.185 fm for Ga and Ge, around 11 % in difference, which is large enough to distinguish these two elements.

4.1.3 Scanning electron microscopy

Scanning electron microscopy (SEM) is a non-destructive technique, producing images of a sample surface at nanometer scale, so the microstructure of the materials can be evaluated. During the experiment, the sample surface is bombarded with high-energy electrons, which further interact with atoms so that secondary electrons (SE) and backscattered electrons (BSE) are emitted. By collecting these electrons, different types of images are produced.

Secondary electron image provides information about the surface topography, with few nanometers in probing depth. Backscattered electrons consist of high-energy electrons originating from the electron beam which are reflected or backscattered from the specimen, approximately 100 nanometers in probing depth. The signal of BSE is related to the atomic number of the sample, heavy elements backscatter electrons more strongly so show higher brightness in the BSE image. Therefore, BSE can detect the difference between areas with different compositions. In order to determine the exact composition, energy-dispersive X-ray fluorescence analysis (EDX) is usually supplemented in the SEM instrument.

Figure 4.2 illustrates both BSE and SE images on the same area of a $Ba_8Al_xGa_{16-x}Ge_{30}$ sample. In the BSE image, the majority area is bright, while some particles along the crack are darker, meaning these particles have different composition than the main phase. EDX analysis further confirmed that these particles are elemental Ge impurity, while the main phase is $Ba_8Al_{4.7}Ga_{11.0}Ge_{30.7}$. As SE image contains information about the surface topography, scratches resulting from polishing can be clearly observed, but in BSE image they are not visible.

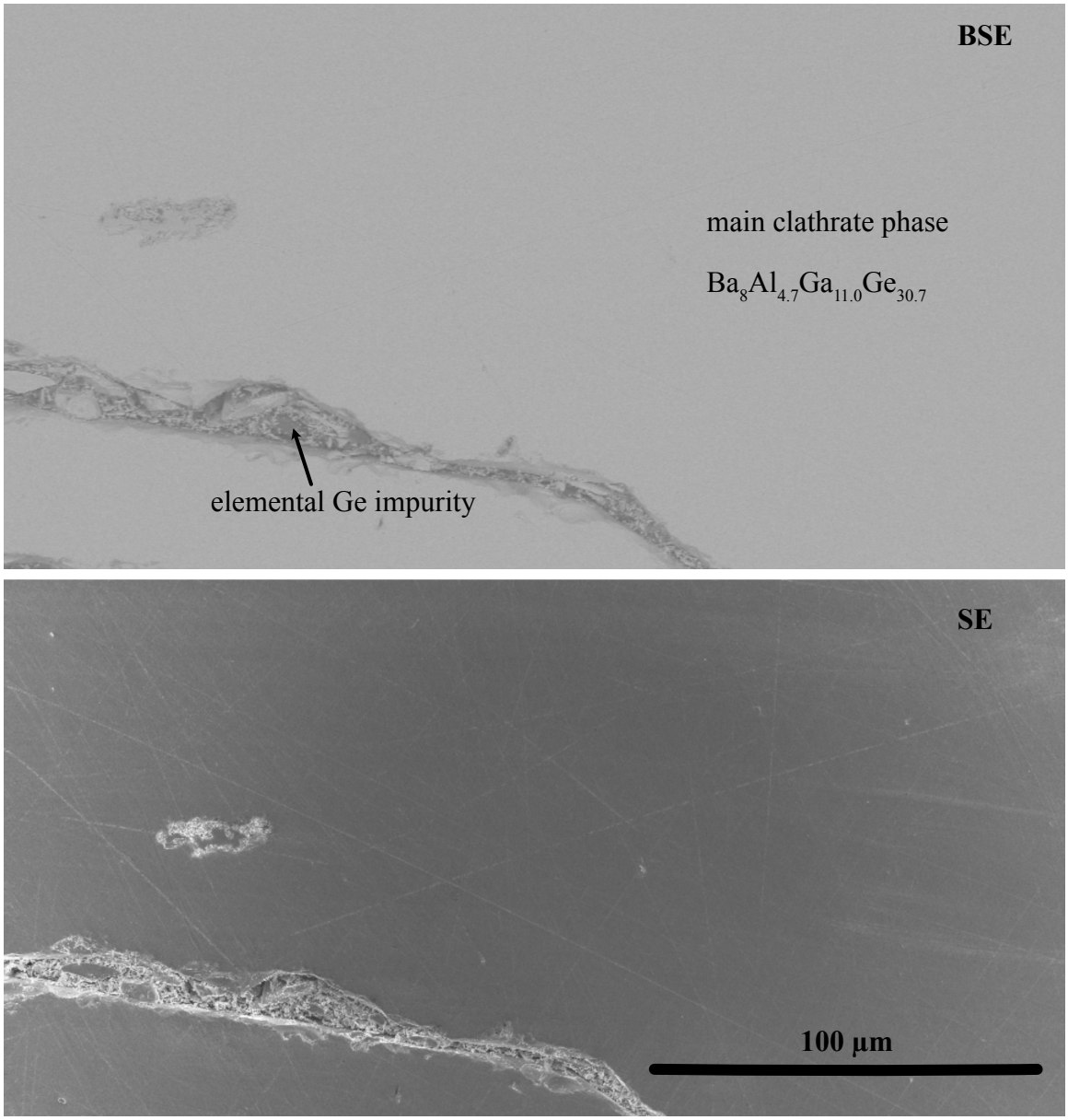

Figure 4.2: *SEM image for a $Ba_8Al_xGa_{16-x}Ge_{30}$ sample, containing a backscattered electron image (BSE) and a secondary electron image (SE) on the same area. The scale bar is 100 µm. Compositions were determined by energy-dispersive X-ray fluorescence analysis (EDX).*

4.1.4 X-ray fluorescence

When a sample is bombarded with high-energy X-ray beam, electrons from the inner orbitals can be excited, and leave 'holes' in the inner orbitals. The electronic structure of such atoms is unstable, so electrons from the higher orbitals 'fall' into the inner and fill in the holes. Meanwhile energy is released in the form of X-ray, which is equal to the energy difference between these two orbitals involved. This phenomenon is X-ray fluorescence. Each element has its own characteristic X-ray

emission spectrum. By detecting the spectrum, the composition of the specimen can be quantified.

X-ray fluorescence analysis (XRF) consists of two methods, energy-dispersive (EDX) and wavelength-dispersive X-ray spectroscopy (WDX). EDX is implemented in SEM and measures the whole spectrum, allowing a quick and semi-quantitative analysis of the composition. WDX measures the emitted X-ray of a single wavelength and has higher spectral resolution, so it can distinguish the elements whose characteristic X-ray peaks are too close to be resolved by EDX. In addition, the detection limit of WDX is lower than that of EDX, 100 - 500 ppm compared to 1000 - 5000 ppm.

In **Paper V**, WDX was used to check the existence of Ce in $Ba_8Al_xGa_{16-x}Ge_{30}$ and to determine its amount. The Ce Kα characteristic peak is explicitly observed in the WDX spectrum (Figure 4.3), and the content is less than 0.4 at. %. In contrast, peaks of Ce and Ba totally overlap in the EDX spectrum, so Ce cannot be determined by EDX at all.

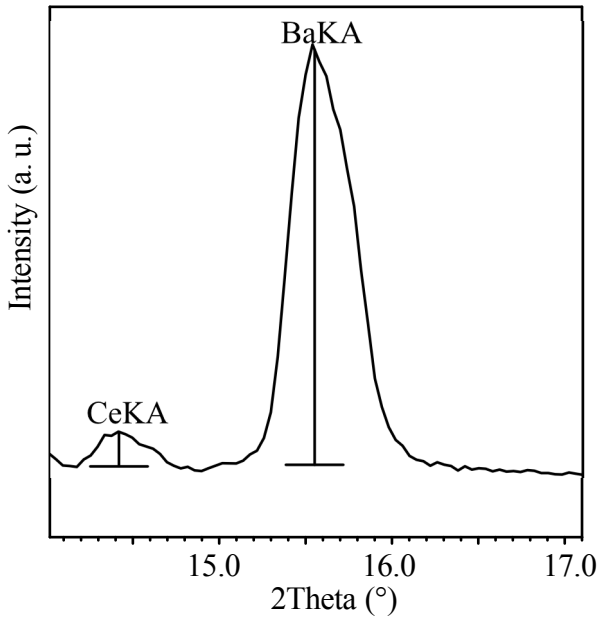

Figure 4.3: *XRF spectrum for the Ce-doped $Ba_8Al_xGa_{16-x}Ge_{30}$ sample. Both Ba Kα and Ce Kα characteristic peaks are observed.*

4.2 Thermoelectric properties analysis

4.2.1 Electrical resistivity and Seebeck coefficient

Electrical resistivity (ρ) and Seebeck coefficient (S) are simultaneously measured by the ZEM3 instrument (Ulvac). A rod-shaped sample (minimum required size $2 \times 2 \times 8$ mm^3) is inserted between two Pt electrodes, and another two probes are

slightly attached to the sample on the side (Figure 4.4). In order to protect the electrodes and probes and also avoid contamination, graphite paper is inserted between them and the sample. The whole sample chamber is in the low-pressure helium atmosphere during the heating.

The schematic of ZEM3 instrument is shown in Figure 4.4. A constant current is passing through the sample during the measurement of ρ, meanwhile the voltage between the two probes is measured. Dividing the voltage by the constant current, the resistance between the probes is calculated. With the known cross-sectional area of the specimen and the distance between two probes, the resistivity of the specimen is finally determined.

During the measurement of S, bottom electrode is heated so a thermal gradient is created along the sample. The probes are able to measure the voltage and temperature simultaneously, and the Seebeck coefficient is calculated according to Equation 2.3. In order to improve the accuracy, at each temperature sample is measured for three times with different temperature gradients and the final result is the average of these three.

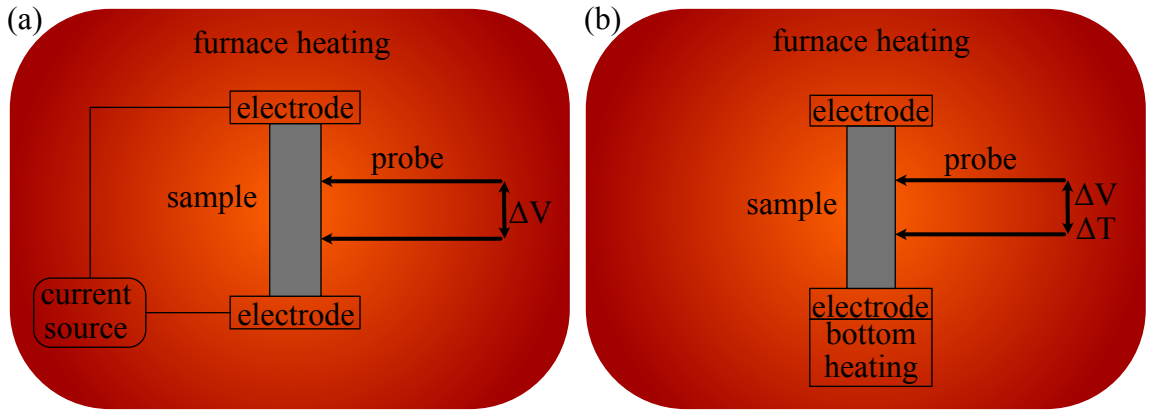

Figure 4.4: *Schematic of ZEM3 instrument for the measurements of (a) electrical resistivity, (b) Seebeck coefficient.*

4.2.2 Weighted charge carrier mobility

Weighted charge carrier mobility (μ_w) was proposed recently,[19] which can be used to estimate the charge carrier mobility (μ). Unlike μ which is usually measured by Hall effect via Physical Property Measurement System (PPMS) instrument, μ_w is calculated directly from the measured resistivity and Seebeck coefficient:

$$\mu_w = \left(\frac{331}{\rho}\right)\left(\frac{T}{300}\right)^{-3/2}\left[\frac{\exp\left[\frac{|S|}{k_B/e}-2\right]}{1+\exp\left[-5\left(\frac{|S|}{k_B/e}-1\right)\right]}+\frac{\frac{3}{\pi^2}\frac{|S|}{k_B/e}}{1+\exp\left[5\frac{|S|}{k_B/e}-1\right]}\right] \quad (4.3)$$

Here k_B is the Boltzmann constant and e is the elementary charge.

With μ_w, the electron transport behavior can be analyzed easily, especially at high temperature. Moreover, materials with low charge carrier mobility is difficult to be measured by PPMS because the signal is weak, but μ_w does not have such limitation.

Weighted charge carrier mobility is used in this thesis to estimate the electron transport mechanism in clathrates. In order to check the validity of μ_w in clathrates, we have calculated μ_w of our samples in comparison with previous reported values (Figure 4.5). It is found that μ_w of our $Ba_8Ga_{16}Ge_{30}$ sample is consistent with the reference values, within 7 % uncertainty. Considering that the Hall effect measurement uncertainty is within 10 - 20 %, thus, μ_w is validated and can show a reasonable estimation of the charge carrier mobility in clathrates. [19]

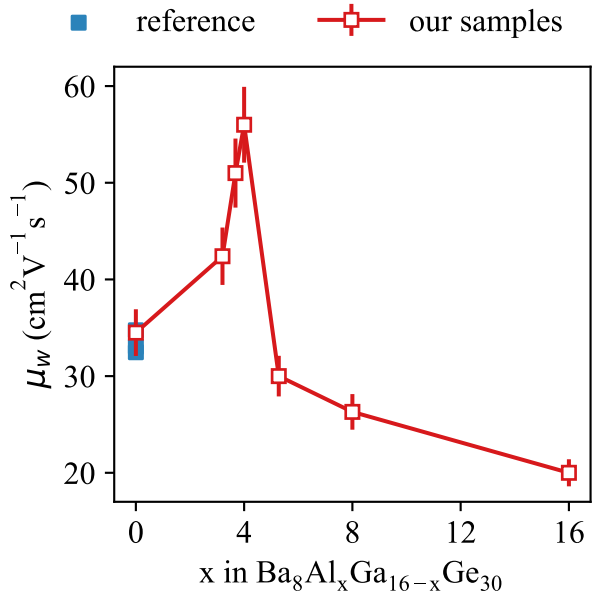

Figure 4.5: *Weighted charge carrier mobility (μ_w) of our $Ba_8Al_xGa_{16-x}Ge_{30}$ samples compared to values from the reference.[57] Error bars refer to 7 % uncertainty.*

4.2.3 Thermal conductivity

Hot Disk TPS 3500 is used to measure the thermal conductivity by the transient plane source technique.[58] Hot Disk sensors consist of a thin layer of double spiral made of nickel, and two sheets of electrically insulating materials sandwiching the nickel film. Because nickel has a Curie temperature of 627 K, the thermal conductivity data cannot be obtained near this temperature. Different modes can be used to measure the thermal conductivity: standard mode requires two identical samples, singe-side measurement needs one sample and a thermally insulating material, thin-film mode can be used when the measured sample is thin film.

To ensure a successful measurement, suitable sensor size and sample size is required, because of the probing depth. Probing depth (Δp) is related to the thermal diffusivity (λ) of the measured sample, and the measurement time (τ): $\Delta p = 2\sqrt{\lambda\tau}$. For high-temperature measurement, minimum measurement time is 1 s, so for clathrates ($\lambda \approx 1$ mm^2/s) the minimum probing depth is 2 mm. That means, the sample should be at least 2 mm in thickness, and the radius of the sample should be 2 mm larger than the radius of the sensor.

During the measurement, sensor serves as both a heater and a temperature sensor: a precise amount of heat is generated in the sensor, meanwhile, the resistance of the sensor is measured using a four-probe setup so the temperature can be converted from the resistance by the known temperature coefficient of resistivity (TCR) of nickel. The recorded resistance of the sensor is:

$$R(t) = R_0 \cdot \left[1 + \alpha \cdot \triangle T_i + \alpha\overline{\triangle T(\tau)}\right] \tag{4.4}$$

Here, R_0 and α are the resistance of the sensor before the measurement and the TCR, respectively. $\triangle T_i$ is the temperature difference between sensor and the thin insulating layer, which becomes constant after a very short time. $\overline{\triangle T(\tau)}$ is the time dependent temperature increase of the sample surface. The expression can be rewritten as:

$$\overline{\triangle T(\tau)} + \triangle T_i = \frac{1}{\alpha}\left[\frac{R(\tau)}{R_0} - 1\right] \tag{4.5}$$

The theoretical temperature increase of the sample surface is related to the thermal conductivity κ of the sample:

$$\overline{\triangle T(\tau)} = \frac{P_0}{\pi^{1.5} \cdot r \cdot \kappa} D(\tau) \tag{4.6}$$

where P_0 and r denote the heating power and radius of the sensor, respectively. κ is the thermal conductivity of the tested sample and $D(\tau)$ is a dimensionless time-dependent function which includes the thermal diffusivity and specific heat capacity of the tested sample. Therefore, the plot of $D(\tau)$ against $\overline{\triangle T(\tau)}$ should be a straight line, from which the slope of the straight line can be calculated, and κ of the sample is determined.

4.2.4 Specific heat capacity

Specific heat capacity (c_p) is measured with a differential scanning calorimetry (DSC) instrument (Mettler Toledo) using the sapphire method (E1269 - 11). Three experiments are performed, measuring the heat flow of an empty crucible, of a crucible with the specimen, and of a crucible with a sapphire standard, respectively. c_p of the specimen is calculated by:

$$c_p = \frac{H_{sample} - H_{crucible}}{m_{sample}} \cdot \frac{m_{sapphire}}{H_{sapphire} - H_{crucible}} \cdot c_p(sapphire) \tag{4.7}$$

Here, H is the heat flow for each measurement and m is the mass.

It is critical that the heat capacity of the measured sample ($c_p \cdot m$) should be close to that of the sapphire standard, in order to obtain accurate results. Selecting a correct crucible is also important, the crucible should have excellent thermal conductivity, and meanwhile it must not react with the measured sample. Sample bottom should be flat and in good contact with the crucible, so the heat can conduct to the sample efficiently.

5 Atomic structure engineering in clathrates

5.1 Host structure elements

5.1.1 Chemical ordering in host structure

Controlling the chemical ordering enables tuning the electrical transport properties, which is a crucial capacity in the semiconductor field in general and for thermoelectric materials in particular.[51] Specifically, the chemical ordering in clathrates refers to the occupation of the host sites $6c$, $16i$ and $24k$, by chemically distinct atoms, *e.g.* Al, Ga and Ge in $Ba_8Al_xGa_{16-x}Ge_{30}$. In order to study the chemical ordering, the local chemical environment of each element needs to be investigated. In **Paper III**, a combination of X-ray and neutron diffraction was employed, using the methodology outlined below.

Single crystal samples were synthesized by either Czochralski method or Ga-flux method[59], and then characterized by single crystal X-ray diffraction (XRD). Since Ga and Ge have similar X-ray cross sections, only the Al site occupation factors (SOFs) were refined. All sites are assumed to have isotropic atomic displacement parameters (ADPs) and be fully (100 %) occupied, but anisotropic ADPs is modeled for the Ba atoms at the $6d$ site. The composition obtained from the structure refinement was further compared with that from X-ray fluorescence analysis (XRF). It was found that compositions obtained from both methods are consistent within the measurement uncertainty, therefore the structural model was validated.

Next, the SOFs of Ga and Ge were examined by neutron diffraction. The structure refinement was similar to the one described above, but with a few constraints: The SOFs of Al are kept fixed and the number of Ge atoms is set to 30 per unit cell. The physical properties (lattice parameter, ADP and atomic position) obtained from neutron diffraction are comparable to those from XRD, meaning that both structure refinements are reasonable.

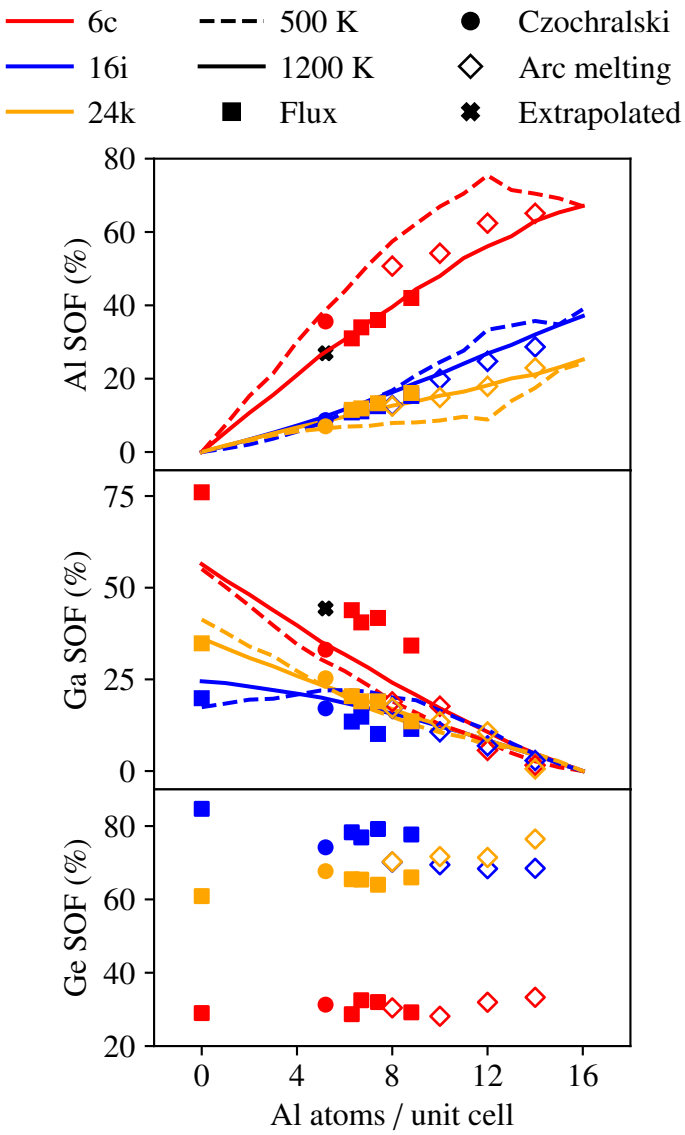

Figure 5.1: *SOFs of the host elements (Al, Ga and Ge) at the 6c (red), 16i (blue), and 24k (orange) sites from experiment (filled circles: Czochralski; filled squares: flux-grown; open diamonds: arc-melted samples [60]) and simulation (dashed lines: 500 K; solid lines: 1200 K). Black crosses indicate SOFs at x=5.2 obtained by extrapolation of the data from flux-grown samples.*

The obtained SOFs for the host elements are shown in Figure 5.1, in comparison with arc-melting samples taken from reference.[60] With the increasing Al content in $Ba_8Al_xGa_{16-x}Ge_{30}$, the Ge SOF at the 6*c* site remains almost constant in the whole composition range, which implies that Ge at the 6*c* site is not substituted by Al at all. By contrast, the Ge SOFs at the other two host sites exhibit large variations: it decreases and increases with Al content, at the 16*i* and 24*k* sites, respectively. This is qualitatively attributed to the fact that the material tends

to avoid direct bonding between trivalent elements. Especially, our theoretical calculations have shown that Al–Al is the least favorable bond and is predicted to be almost absent in $Ba_8Al_xGa_{16-x}Ge_{30}$, while Ga–Ga bonds can be tolerated to some extent. Therefore, with the increasing Al content, 16*i* site is more preferred by Al atoms compared to the 24*k* site, because 24*k* site is directly connected to 6*c* site which is dominant by trivalent elements.

The trivalent elements Al and Ga are found on all the host sites, but preferably occupy the 6*c* site, which is consistent with the empirical rules.[47, 48] Al is found to be nearly equally distributed between the 16*i* and 24*k* sites, while Ga shows a higher preference for the 24*k* site. This also corresponds well with the conclusion that, the materials tend to avoid Al–Al and also Al–Ga bonds. Interestingly, the occupation of the 6*c* site differs between samples synthesized by different methods, as the Al (Ga) occupation at the 6*c* site in the Czochralski and arc-melted [60] samples are systematically higher (lower) than those synthesized via the flux method.

5.1.2 Degree of chemical ordering

In terms of thermodynamics, entropy has a larger impact at high temperatures, where it may drive materials that are ordered at low temperatures to form disordered structures. In order to characterize the degree of chemical ordering, atomic scale simulations were performed and the calculated SOFs versus temperature are shown in Figure 5.2. The existence of the order-disorder transition is evident from the temperature variations of the Al and Ga SOFs, respectively, in $Ba_8Al_xGa_{16-x}Ge_{30}$ clathrates ($x = 5$). The SOFs for both elements change dramatically at the order-disorder transition temperature of approximately 400 K and then change gradually until 1200 K, which is close to the melting point.

Comparing the calculated SOFs with our experimental data (Figure 5.2), it is explicitly revealed that our Czochralski sample is consistent with the calculated configuration at 500 K, while the extrapolated SOFs of the flux-grown sample correspond better to the high-temperature configuration. If extending this analysis over a wider composition range ($0 \leq x \leq 14$ in $Ba_8Al_xGa_{16-x}Ge_{30}$), as shown in Figure 5.1, it can be concluded that the flux-grown samples are consistent with high-temperature configurations, while the arc-melted and Czochralski samples are between the calculated high-temperature and ground states. In other words, the flux-grown samples are, more disordered compared to the others.

In summary, we have proved that the degree of chemical ordering differs between samples synthesized by different methods, because the materials reach different equilibration during the reaction. This, in turn, offers new handle to design the material and also tune the thermoelectric properties, by adjusting the annealing temperature, cooling rate and chemical environment.

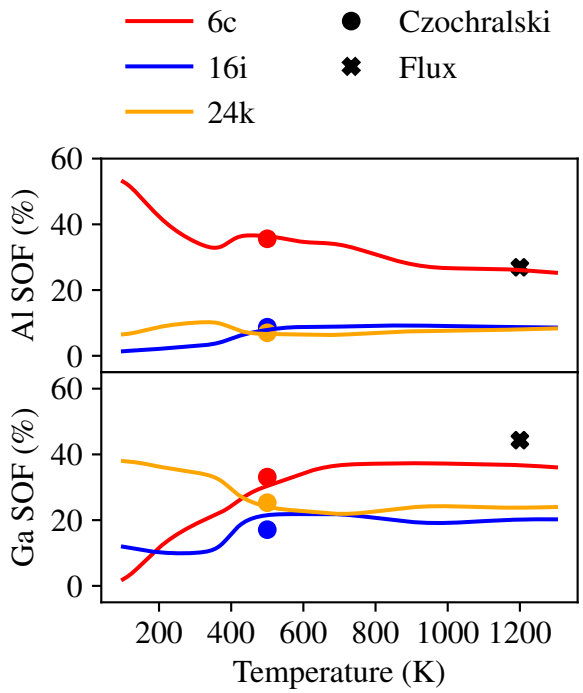

Figure 5.2: *Variation of the simulated Al and Ga SOFs with temperature at the 6c (red), 16i (blue) and 24k (orange) Wyckoff sites for* $Ba_8Al_xGa_{16-x}Ge_{30}$ *(x=5), together with experimental data points for the Czochralski sample (filled circles) and extrapolated data from flux-grown samples (black crosses).*

5.1.3 Order-disorder transition controls electrical transport properties

Theoretical calculations have shown that the SOFs of the host elements undergo an abrupt change around 400 K, from an ordered ground state to disordered high-temperature configuration. In **Paper II**, it is revealed that this order-disorder transition generally exists in the whole quaternary clathrate series $Ba_8Al_xGa_{16-x}Ge_{30}$. Moreover, this phase transition can influence the electrical conductivity and Seebeck coefficient by altering the band structure.

In order to confirm the order-disorder phase transition, specific heat capacity (c_p) of $Ba_8Al_xGa_{16-x}Ge_{30}$ samples was determined by differential scanning calorimetry (DSC), and the result is shown in Figure 5.3. The Dulong-Petit estimation of c_p is 0.361, 0.382 and 0.426 $Jg^{-1}K^{-1}$ for samples $x = 0, 5$ and 16, respectively,[57] and our experimental data is consistent with these estimations considering the fact that the measurement uncertainty is 10 % for the sapphire method. The order-disorder transition is unambiguously evidenced by two features: the discontinuity (sharp λ-shaped feature) which occurs around 600 K to 650 K for all these three samples, and the difference in specific heat capacity below and above the transition temperature (Δc_p). It should be noted that our

experimental results also agree qualitatively with the theoretical calculations. Therefore, the existence of the order-disorder transition is corroborated both experimentally and theoretically in $Ba_8Al_xGa_{16-x}Ge_{30}$ clathrates.

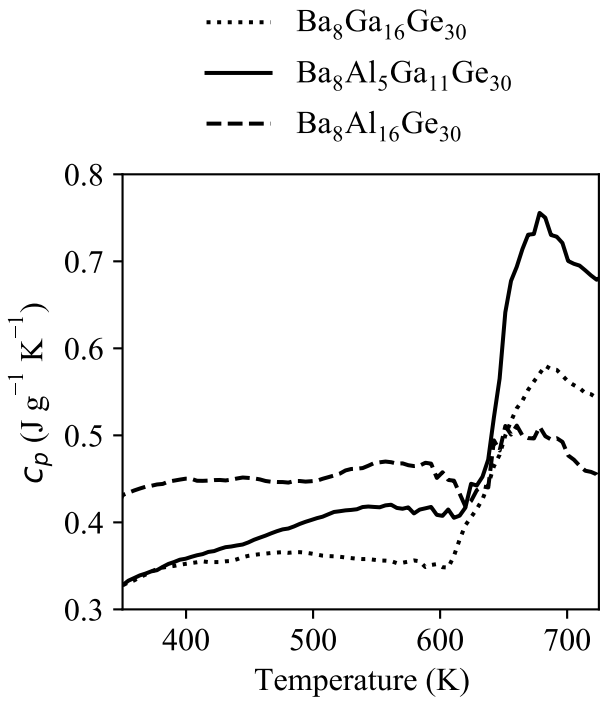

Figure 5.3: *Measured c_p for $Ba_8Al_xGa_{16-x}Ge_{30}$ samples with x=0, 5 and 16, respectively.*

To scrutinize the effect of order-disorder transition on the electrical transport properties, the experimental and calculated data is compared and shown in Figure 5.4. Taking the order-disorder transition into account, better agreement is achieved since the data for the HT structures match the measurements better above 700 K. Interestingly, the slope of the Seebeck coefficient increases sharply at a specific temperature for all three compositions. On the other hand, it is only $Ba_8Al_{16}Ge_{30}$ that exhibits a distinct feature, in the form of a sharp increase in the electrical conductivity (σ) at the same temperature. It has been further pointed out that, the effect of the order-disorder phase transition on the electrical transport properties results from the change in the band structure, more specifically, the density of states (DOS) near the Fermi level. DOS for the HT configuration is enhanced for both $Ba_8Ga_{16}Ge_{30}$ and $Ba_8Al_5Ga_{11}Ge_{30}$, which explains the sharp increase in the Seebeck coefficient. While for $Ba_8Al_{16}Ge_{30}$, a similar trend appears slightly far away from the Fermi level, that is why the electrical conductivity is enhanced for HT compared to GS configuration.

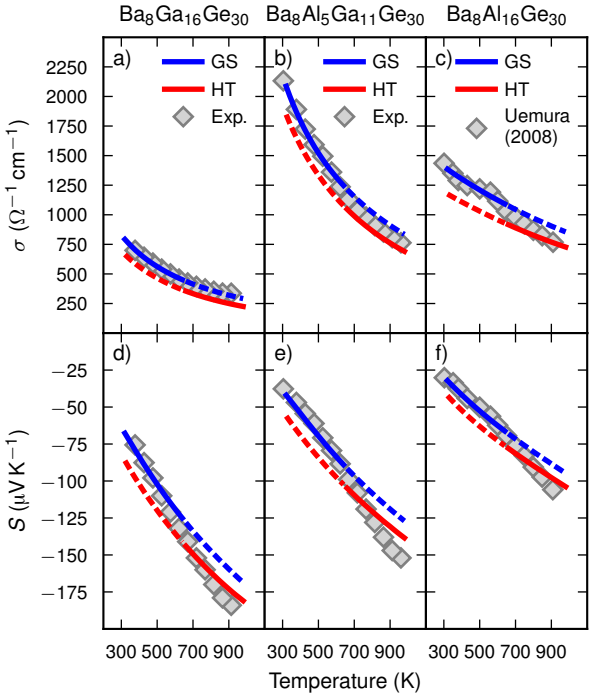

Figure 5.4: *(a-c) Electrical conductivity and (d-f) Seebeck coefficient as a function of temperature. The calculated results for the ground state (GS) and high-temperature state (HT) structures have been plotted as blue and red lines, respectively, while the gray diamonds represent data from experiments.*

5.2 Atomic vacancies

Atomic vacancies play a crucial role in electrical transport: they can either scatter electrons (or holes in p-type materials) and reduce the charge carrier mobility, also change the charge balance and shift the Fermi level. In **Paper IV**, we found that atomic vacancy content is closely related to the Al/Ga ratio in $Ba_8Al_xGa_{16-x}Ge_{30}$. The atomic vacancy affects the electrical transport properties by altering the electron scattering mechanism, and moreover, induces a semiconducting-to-metallic transition, which has been reported previously but not yet been explained. [57]

5.2.1 Characterization of atomic vacancies

$Ba_8Al_xGa_{16-x}Ge_{30}$ samples ($x < 8$) were synthesized by Ga-flux method and sintered to pellet via spark plasma sintering (SPS). Detailed single crystal XRD and XRF analysis have confirmed that the exact composition for the sample (Al = 0) should be $Ba_8Ga_{15.4}Ge_{30}$, meaning that the material contains atomic vacancies. In order to check if other samples also contain vacancies, the lattice parameters are compared together with data from the references. [47, 48] As shown in

Figure 5.5, the lattice parameter of $Ba_8Al_xGa_{16-x}Ge_{30}$ generally increases with the number of Al atoms, consistent with the fact that $Ba_8Al_{16}Ge_{30}$ has larger unit cell than $Ba_8Ga_{16}Ge_{30}$. Therefore, based on Vegard's law, the lattice parameter of $Ba_8Al_xGa_{16-x}Ge_{30}$ should be within the orange area as indicated in Figure 5.5. However, the lattice parameters of two samples (Al = 3.4 and Al = 4.5) significantly deviate from this trend, and in fact, the corresponding unit cells are even smaller than that of $Ba_8Ga_{16}Ge_{30}$, which indicates that samples with low Al content (Al < 5) may contain atomic vacancies in the unit cell.

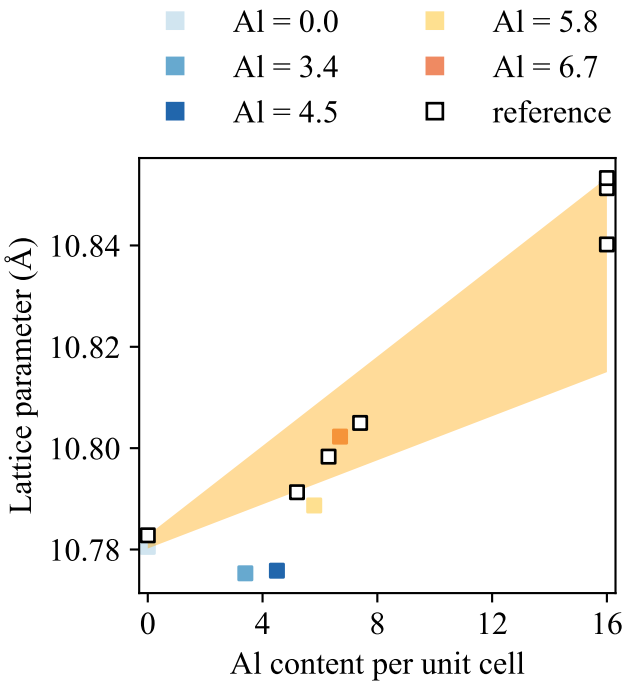

Figure 5.5: *Lattice parameters (filled squares) of the as-synthesized crystals. Sample's name indicates the number of Al atoms per unit cell, which is determined from structure refinement of XRD. Empty squares are the lattice parameters of* $Ba_8Al_xGa_{16-x}Ge_{30}$ *taken from the literature.[47, 48]*

The most compelling evidence for the atomic vacancies comes from the analysis of the weighted charge carrier mobility (μ_w). As shown in Figure 5.6a, μ_w of these five samples, at a fixed temperature (373 K), increases with the Al content. As mentioned above, atomic vacancies can scatter electrons and thus reducing the charge carrier mobility. Therefore, it indicates that the atomic vacancies are partially filled with the Al atoms, until Al is more than 5 atoms per unit cell.

The electron scattering mechanism, which can be reflected by the temperature dependence of μ_w, also lends the support, as shown in Figure 5.6b. Since the sample Al = 0.0 contains atomic vacancies as confirmed by the structure and composition analysis, these vacancies lead to locally-unbalanced charges and thus

gives rise to ionized impurity scattering (IIS). The charge carrier mobility $\mu \propto T^{3/2}$ for IIS, and the experimentally observed $\mu_w \propto T^{1.31}$, which is relatively close considering the measurement uncertainty. At higher temperature, $\mu_w \propto T^{-3/2}$ for the sample Al = 0.0, which is the typically acoustic phonon scattering (APS) behavior and consistent with previous study.[57] Once Al is introduced into the host structure and Ga is substituted by this isovalent element, the alloy scattering should also be taken in account. With $\mu_w \propto T^{1.14}$ and $\mu_w \propto T^{0.60}$ at low temperatures for Al3.4 and Al4.5, respectively, we expect that both IIS and alloy scattering are taking place, which can be seen as indirect evidence for the existence of vacancies.

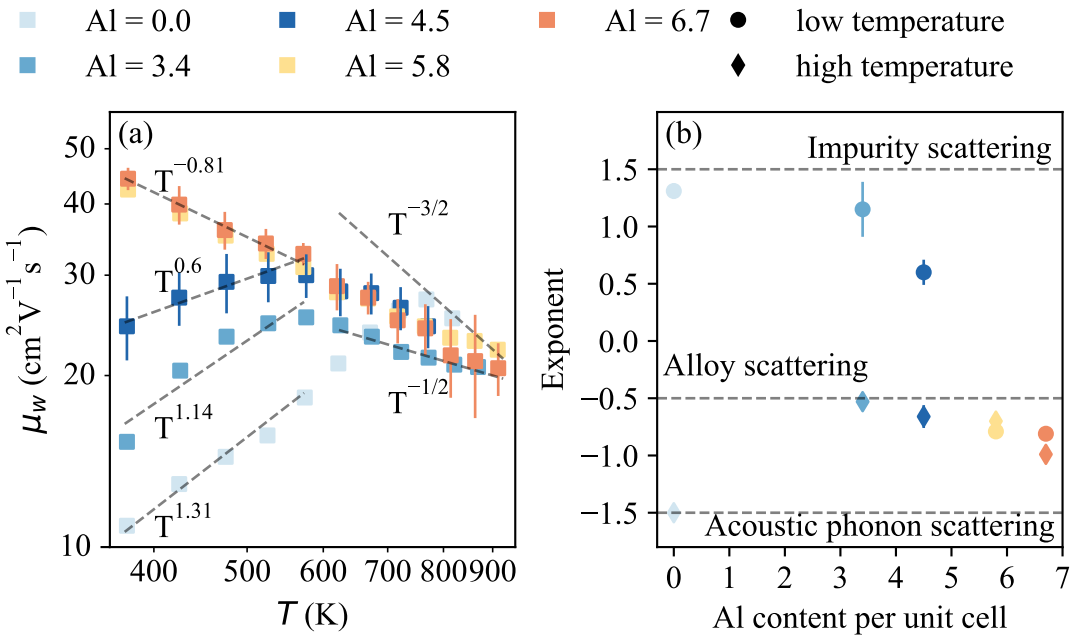

Figure 5.6: *(a) Weighted charge carrier mobility (μ_w) versus absolute temperature plotted on a log-log scale, for $Ba_8Al_xGa_{16-x}Ge_{30}$ samples Al = 0.0 (pale blue); Al = 3.4 (light blue); Al = 4.5 (dark blue); Al = 5.8 (yellow); and Al = 6.7 (orange). The dashed lines indicate the temperature dependence. The averaged standard deviation is 10 % and 6 % for samples Al = 4.5 and Al = 6.7, respectively. (b) Temperature exponents of μ_w at low and high temperature. Dashed lines indicate the exponents for IIS, alloy scattering and APS, respectively. The error bar is the standard error obtained from the regression.*

5.2.2 Vacancy-induced semiconducting-to-metallic transition

The order-disorder phase transition implies that the host atoms become increasingly mobile at elevated temperature. If the unit cell contains atomic vacancies, the atomic rearrangement can be expected to be more complex.

The measured resistivity and Seebeck coefficient are shown in Figure 5.7a and c.

The vacancy-free samples Al = 5.8 and 6.7 show n-type degenerate semiconducting behavior, with negative Seebeck coefficient and that the resistivity increases with temperature. On the other hand, the vacancy-containing sample Al = 4.5 exhibits a semiconducting-to-metallic transition in the resistivity: ρ initially decreases with temperature like an intrinsic semiconductor, but around 500 K it increases abruptly and its temperature dependence also changes oppositely, until 800 K when the bipolar effect occurs and both the resistivity and the absolute value of the Seebeck coefficient start to decrease. It should be noted that this peculiar transition has been observed previously, but not yet explained.[57]

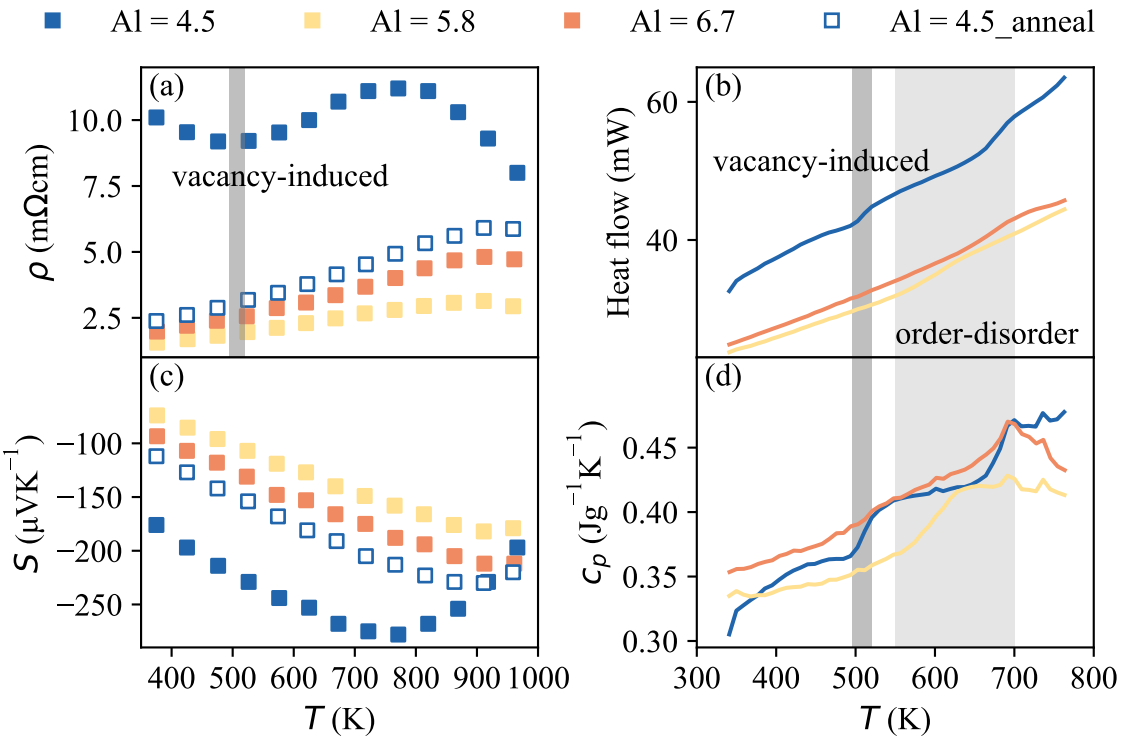

Figure 5.7: *(a) Resistivity and (c) Seebeck coefficient for sample Al = 4.5 before (blue filled markers) and after (blue unfilled markers) annealing, together with data for the vacancy-free samples. (b) Heat flow and (d) specific heat capacity for samples Al = 4.5 (dark blue); Al = 5.8 (yellow); and Al = 6.7 (orange). The vacancy-induced and order-disorder transitions are marked by the dark and light gray areas, respectively.*

In order to study this transition in more depth, c_p was determined via DSC and is plotted in Figure 5.7b and d together with the measured heat flow. An endothermic peak around 600 K to 700 K is observed for all samples, which further leads to the discontinuity in c_p and Δc_p before and after the transition temperature. This transition, as is discussed in **Paper II**, corresponds to the order-disorder phase transition in the host elements. Surprisingly, another endothermic peak is observed for the sample Al = 4.5 solely, which occurs at the

same temperature (500 K) as the abrupt change in the resistivity. This implies that another phase transition may occur in the vacancy-containing sample, which possibly induces the semiconducting-to-metallic transition in the resistivity.

5.2.3 Suppressing vacancy improves electron transport

In order to eliminate the atomic vacancy, sample Al = 4.5 was further annealed at 973 K for 5 days. It is found that after annealing, the peculiar transition disappears and the sample behaves just like other vacancy-free samples, as shown in Figure 5.7a and c. By analyzing μ_w of the annealed sample (Figure 5.8), it is also confirmed that the vacancy is suppressed, which further lends the support that the semiconducting-to-metallic transition is indeed induced by the atomic vacancies. Comparing μ_w of these vacancy-free samples (Al = 4.5 after annealing, Al = 5.8 and 6.7), it is found that μ_w is almost identical and all these three samples have the same electron scattering mechanism, a mixing mechanism between alloy scattering and APS ($\mu_w \propto T^{-0.8}$). Therefore, it is concluded that, by suppressing the atomic vacancy in $Ba_8Al_xGa_{16-x}Ge_{30}$ (high-temperature annealing or adjusting Al/Ga ratio), the charge carrier mobility has been tuned to an optimal level.

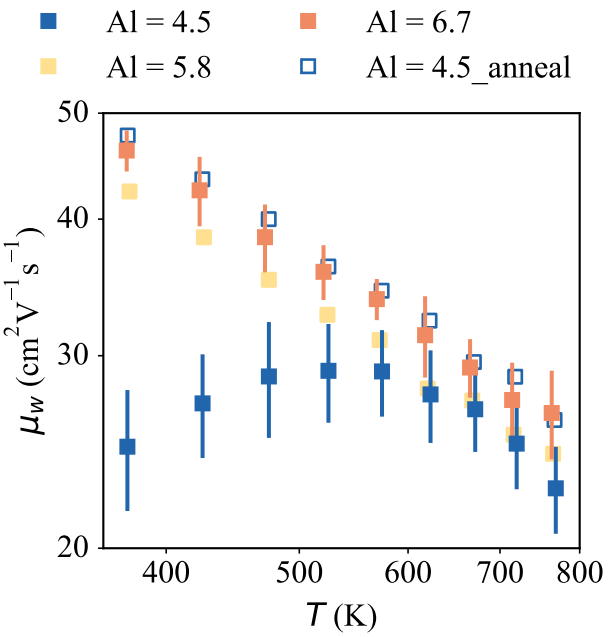

Figure 5.8: *Weighted charge carrier mobility for sample Al = 4.5 before (blue filled markers) and after (blue unfilled markers) annealing, together with data for the vacancy-free samples.*

Thermal conductivity (κ), power factor (PF) and figure of merit (zT) are shown in Figure 5.9. Benefiting from the improved electron transport, all the vacancy-free samples show superior PF than the vacancy-containing sample (Al

= 4.5). However, due to atomic vacancies the sample Al = 4.5 exhibits the lowest κ, while the sample Al = 5.8 shows the highest thermal conductivity because of the high electronic contribution. As a result, the best combination between electron and phonon transport is achieved for sample Al = 6.7, whose zT reaches 0.7 at 873 K.

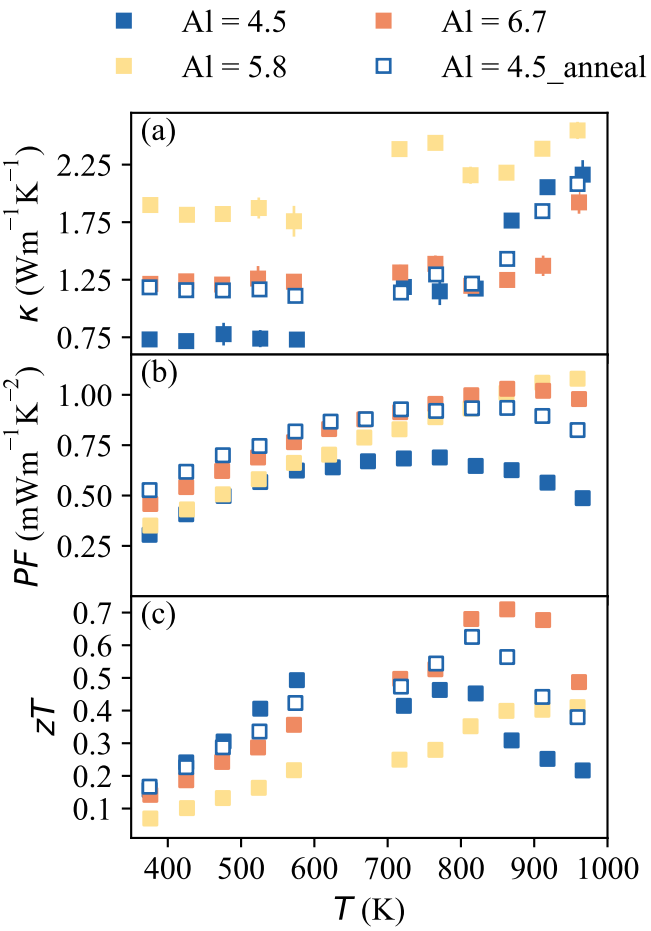

Figure 5.9: *(a) Thermal conductivity (κ), (b) power factor (PF) and (c) figure of merit (zT) for samples Al = 4.5 (dark blue); Al = 5.8 (yellow); Al = 6.7 (orange); and annealed Al = 4.5 (dark blue unfilled markers).*

5.3 Guest atoms substitution

In **Paper V**, $Ce_yBa_{8-y}Al_xGa_{16-x}Ge_{30}$ samples were synthesized via Ga-flux method, in order to explore the effect of guest atoms substitution. XRF confirms the existence of Ce in the sample, as shown in Figure 4.3. However, the determined Ce content is lower than the expectation: the initial mixing ratio is $Ce_1Ba_7Al_6Ga_{28}Ge_{30}$, but the final determined composition is $Ce_{0.16}Ba_{5.82}Al_{2.60}Ga_{13.04}Ge_{31.19}$. Two Ce-doped samples were successfully

synthesized and the thermoelectric properties were measured, and compared to the undoped samples.

Due to the fact that Ce has two more valence electrons than Ba, doping with Ce is expected to lead to higher carrier concentration, and thus resulting in lower electrical resistivity (ρ) and absolute value of Seebeck coefficient (S) compared to the undoped material, as can be seen in Figure 5.10a and b. Nevertheless, high carrier concentration also leads to higher electronic thermal conductivity and thus the thermal conductivity of the Ce-doped samples is significantly higher than that of the undoped samples (Figure 5.10c). Consequently, zT is not improved by Ce doping, which is, unfortunately, consistent with the suggestion from our theoretical calculations in **Paper IV**.

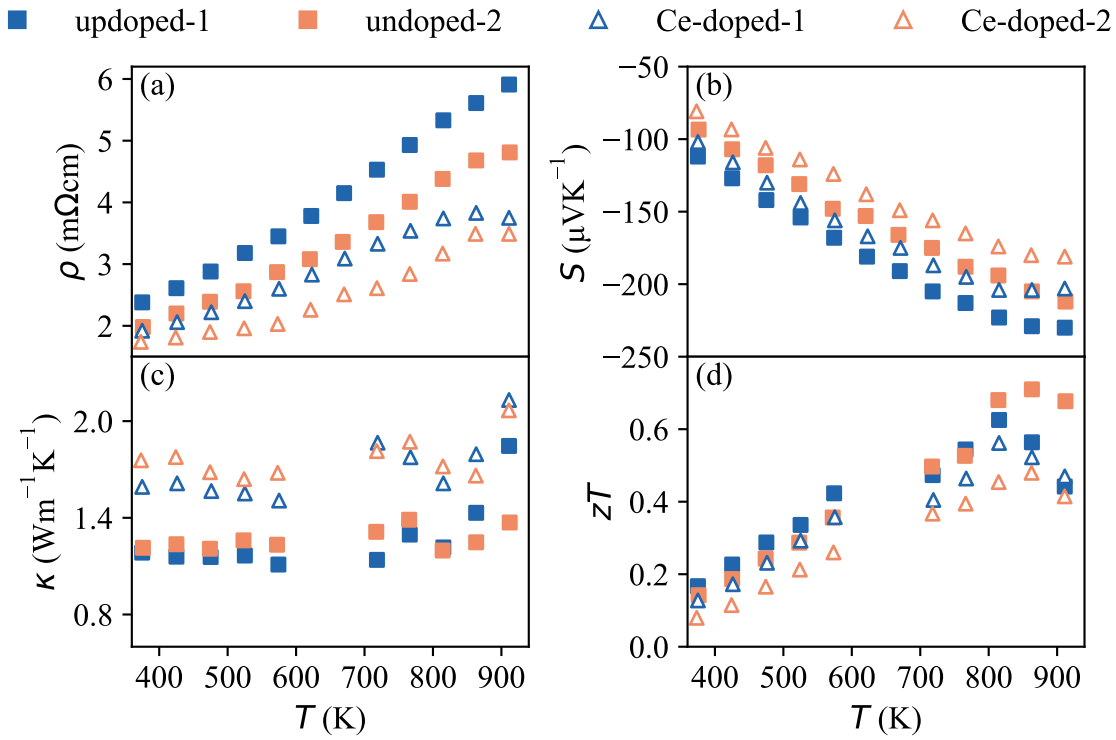

Figure 5.10: *(a) Electrical resistivity (ρ), (b) Seebeck coefficient (S), (c) thermal conductivity (κ) and (d) figure of merit (zT) for Ce-doped and undoped samples. Here, the undoped-1 and undoped-2 samples are the annealed Al = 4.5 and Al = 6.7 from* ***Paper IV****, respectively. The composition of samples Ce-doped-1 and Ce-doped-2 is* $Ce_{0.16}Ba_{5.82}Al_{2.60}Ga_{13.04}Ge_{31.19}$ *and* $Ce_{0.24}Ba_{6.72}Al_{4.70}Ga_{11.16}Ge_{31.18}$*, determined by XRF.*

6 Microstructure engineering in clathrates

From the atomic structure analysis of $Ba_8Al_xGa_{16-x}Ge_{30}$ clathrates, especially Figure 5.8, the charge carrier mobility has already been increased to an optimal level. In order to further improve the thermoelectric performance, several points need to be considered:

1. Al/Ga ratio and atomic vacancy: atomic vacancy reduces charge carrier mobility and therefore needs to be eliminated.

2. high carrier concentration is beneficial because the density of states can be enhanced through order-disorder transition, however, too high doping level leads to high electronic thermal conductivity (κ_e).

3. lattice thermal conductivity (κ_l) has the potential to be reduced further via microstructure engineering.

4. charge carrier mobility needs to be increased further, if possible, by improving the interfaces.

In **Paper I**, a novel method is used to synthesize $Ba_8(Al_xGa_{1-x})_{16}Ge_{30}$ clathrates (the sample name is slightly different in order to differentiate from the flux-grown samples), and the μ_w of the obtained samples is found to be surprisingly higher than that of the single crystal sample. Both the electron and phonon transport is improved (μ_w is increased while κ_l is reduced) by engineering the microstructure, and a greatly improved understanding of the process-structure-property relationship is achieved.

6.1 Synthesis and microstructure

Unlike conventional method where quaternary $Ba_8Al_xGa_{16-x}Ge_{30}$ is synthesized directly, a novel method was employed as shown in Figure 6.1: $Ba_8Ga_{16}Ge_{30}$ and $Ba_8Al_{16}Ge_{30}$ compounds were synthesized initially, and then mixed at certain ratio in a ball-milling setup; the powder mixture was sintered by SPS and finally processed for thermoelectric properties measurements.

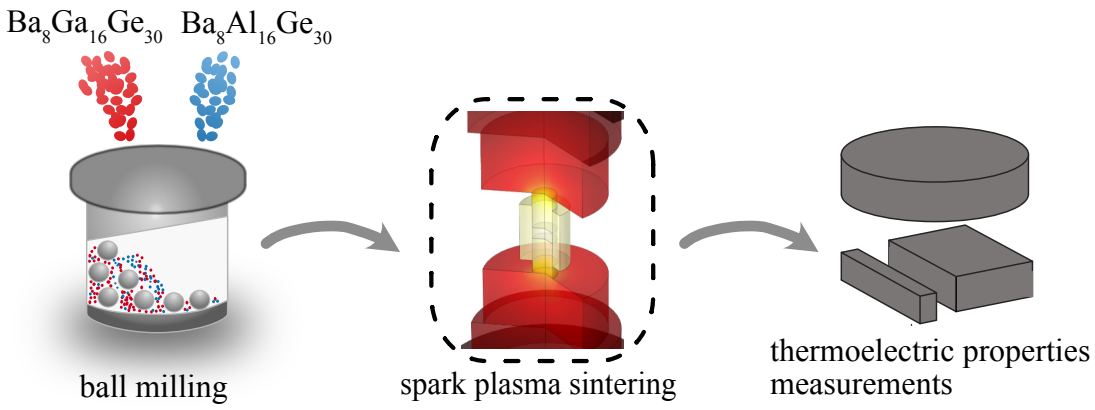

Figure 6.1: *Novel method of synthesizing quaternary $Ba_8(Al_xGa_{1-x})_{16}Ge_{30}$. $Ba_8Ga_{16}Ge_{30}$ and $Ba_8Al_{16}Ge_{30}$ powder is mixed at certain ratio by ball milling, and the mixture is then sintered by SPS and further processed for thermoelectric properties measurements.*

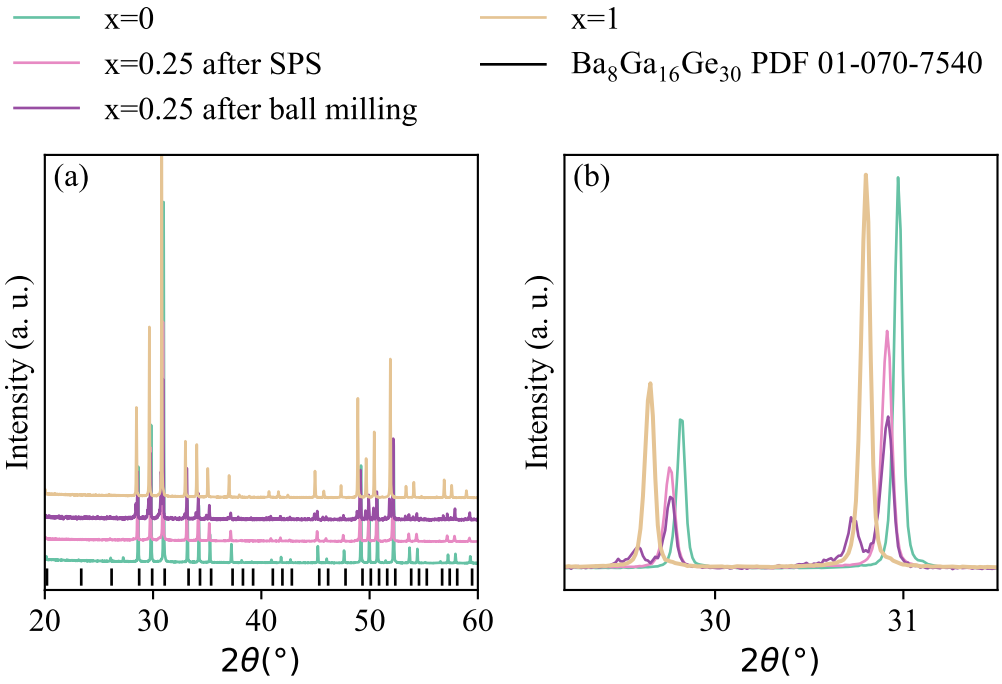

Figure 6.2: *XRD patterns of $Ba_8(Al_xGa_{1-x})_{16}Ge_{30}$ with $x = 0$, 0.25 and 1. (a) 2θ from 20° to 60° and (b) 2θ from 29° to 32°*

Powder XRD was used to check the phase purity of the synthesized $Ba_8(Al_xGa_{1-x})_{16}Ge_{30}$, as shown in Figure 6.2. All samples exhibit the type-I clathrate structure, and the peak position is consistent with the fact

that $Ba_8Al_{16}Ge_{30}$ has larger unit cell than $Ba_8Ga_{16}Ge_{30}$.[47, 48] Interestingly, comparing the sample $x = 0.25$ before and after SPS, it is found that $Ba_8(Al_{0.25}Ga_{0.75})_{16}Ge_{30}$ is partially formed during the mechanical ball milling. It should also be noted that, the XRD analysis did not reveal the existence of any secondary phase.

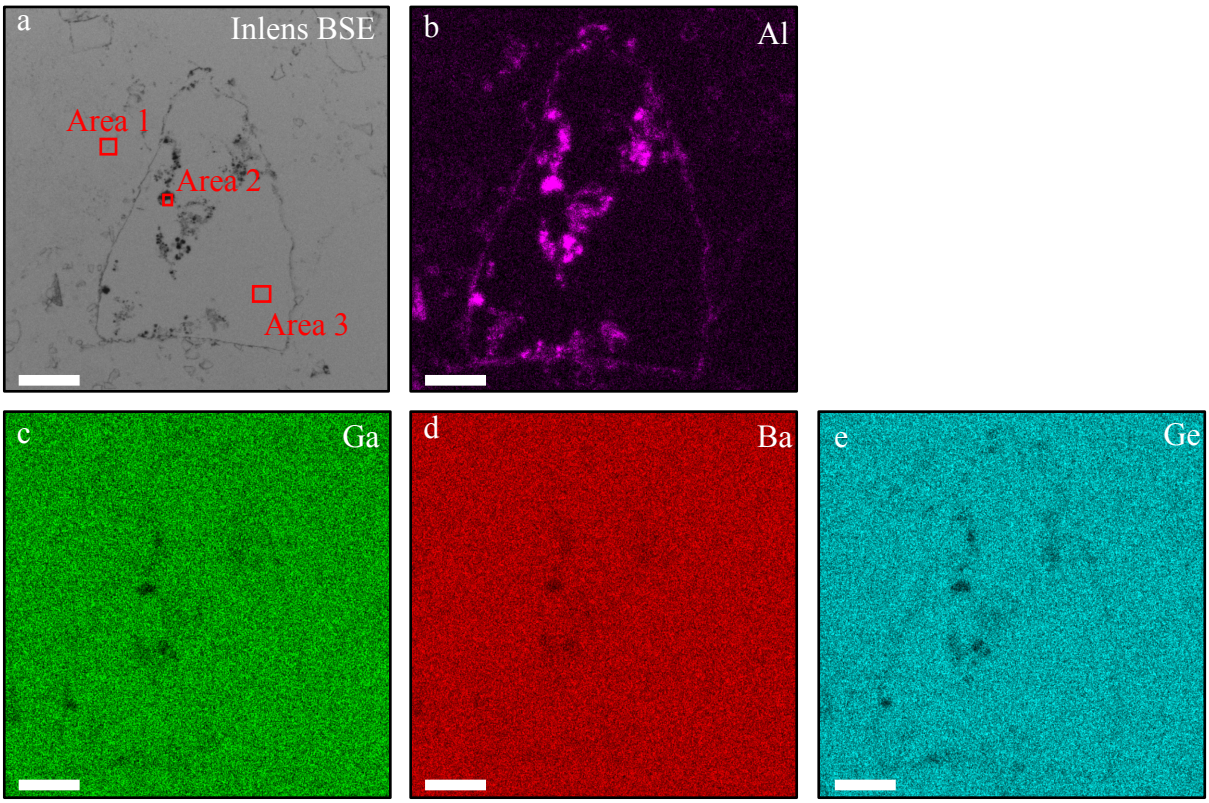

Figure 6.3: *SEM analysis of a clathrate grain in the SPS sintered sample $Ba_8(Al_{0.25}Ga_{0.75})_{16}Ge_{30}$ showing (a) inlens backscattered electron micrograph (BSE), and (b-e) elemental distribution maps of (b) Al, (c) Ga, (d) Ba, and (e) Ge. The average compositions of the selected areas measured by EDX are $Ba_8Al_{2.9}Ga_{11.3}Ge_{28.0}$ (area 1), $Ba_8Al_{77.2}Ga_{23.30}Ge_{29.8}$ (area 2) and $Ba_8Al_{2.8}Ga_{11.9}Ge_{27.9}$ (area 3), respectively. Scale bar is 10 µm.*

SEM/EDX analysis has further revealed that, the microstructure of the sintered $Ba_8(Al_xGa_{1-x})_{16}Ge_{30}$ samples is highly related to the mixing ratio between $Ba_8Ga_{16}Ge_{30}$ and $Ba_8Al_{16}Ge_{30}$. A homogeneous microstructure is discovered for samples with $x \leq 0.2$, while on the other hand, the reaction is not complete for the sample $x = 0.5$ since unreacted $Ba_8Ga_{16}Ge_{30}$ and $Ba_8Al_{16}Ge_{30}$ are observed. Noticeably, a heterostructure is formed for the sample $x = 0.25$, as shown in Figure 6.3. The main phase is still $Ba_8(Al_xGa_{1-x})_{16}Ge_{30}$, as confirmed by the EDX analysis of the area 1 and 3. However, it is evident that Al is not homogeneously distributed throughout the sintered sample, but rather appears in higher concentrations in some areas, which include aggregation at the grain

boundaries and particles inside the grains (area 2).

6.2 Improvement of electron and phonon transport

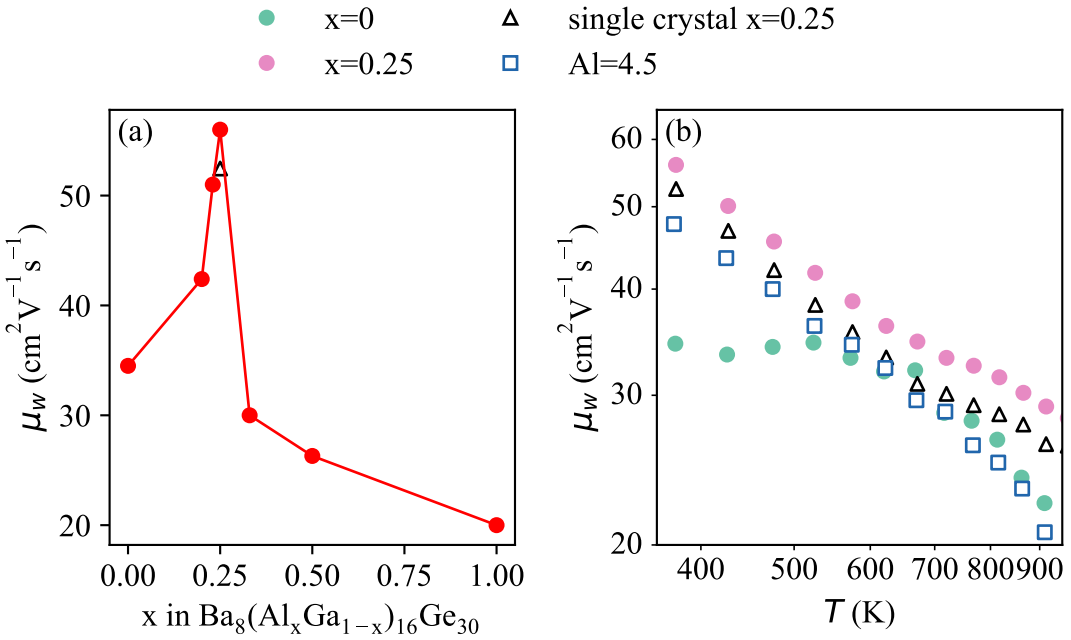

Figure 6.4: *(a) μ_w at 373 K for the $Ba_8(Al_xGa_{1-x})_{16}Ge_{30}$ samples synthesized by alloying $Ba_8Ga_{16}Ge_{30}$ with $Ba_8Al_{16}Ge_{30}$, together with the single crystal synthesized by Czochralski method from* ***Paper III****. (b) μ_w versus absolute temperature plotted in log-log scale, data includes the samples x=0, x=0.25 (alloying 25 at. % $Ba_8Al_{16}Ge_{30}$ with 75 at. % $Ba_8Ga_{16}Ge_{30}$), single crystal x=0.25 (synthesized by Czochralski method from* ***Paper III****) and Al=4.5 (annealed sample Al=4.5 from* ***Paper IV****.)*

Due to the unique microstructure, both the electron and phonon transport is improved for the sample with $x = 0.25$.

As shown in Figure 6.4a, μ_w of the sample $x = 0.25$ is significantly larger than that of other samples, and even higher than that of the single crystal. The charge carrier mobility of the sintered sample should normally be lower than that of the single crystal, because of the grain boundaries. As shown in Figure 6.4b, even though the atomic vacancy is eliminated, μ_w of the sample Al=4.5 is still lower than that of the single crystal. However, we do not observe such behavior for the sample $x = 0.25$. Therefore, we can attribute the greatly enhanced charge carrier mobility to the unique microstructure, which consists of the clathrate main phase and aggregates of Al particles.

The thermal conductivity (κ) of the alloyed $Ba_8(Al_xGa_{1-x})_{16}Ge_{30}$ samples was measured and the lattice thermal conductivity (κ_l) was calculated, as shown in

Figure 6.5. The thermal conductivity of both samples $x = 0$ and Al=4.5 is relatively low, because these two samples are moderately doped (Ge is close to 30 atoms per unit cell) so the electronic contribution is not dominant. On the other hand, two $Ba_8(Al_xGa_{1-x})_{16}Ge_{30}$ samples $x = 0.20, 0.25$ exhibit high thermal conductivity, because they are heavily doped (the composition deviates from the stoichiometric composition).

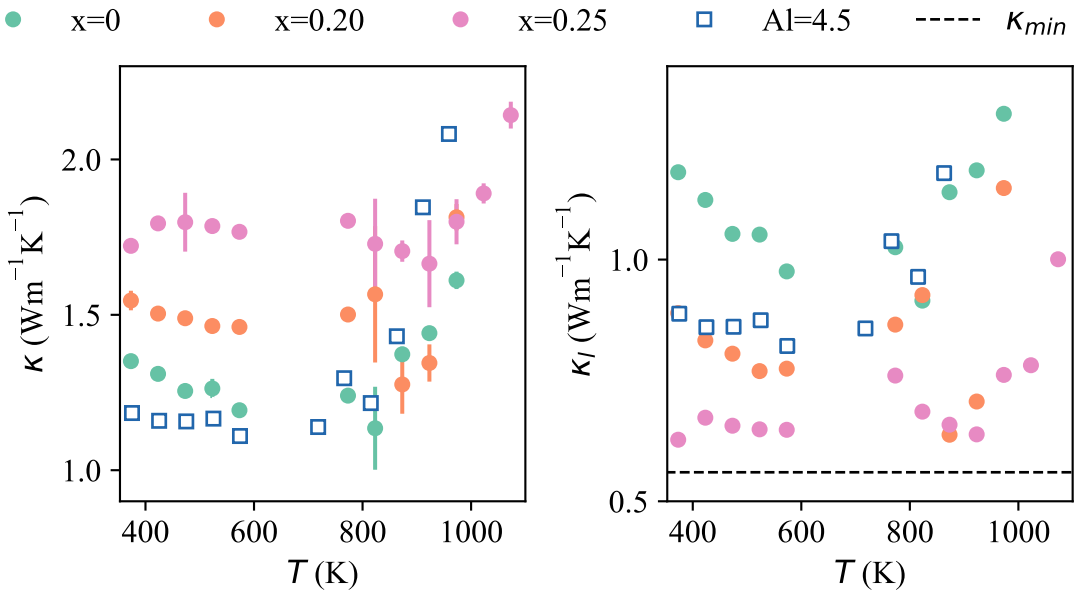

Figure 6.5: *(a) Thermal conductivity (κ) and (b) lattice thermal conductivity (κ_l) of $Ba_8(Al_xGa_{1-x})_{16}Ge_{30}$, $x = 0$, 0.20 and 0.25. κ_{min} refers to the theoretical minimum lattice thermal conductivity of $Ba_8Ga_{16}Ge_{30}$.[57] Sample Al=4.5 is the annealed sample Al=4.5 from* ***Paper IV****.*

If the electronic contribution is ruled out and only the lattice thermal conductivity (κ_l) is compared, as shown in Figure 6.5b, κ_l of all the quaternary clathrates is explicitly lower than the ternary $Ba_8Ga_{16}Ge_{30}$ clathrate, which can be attributed to the alloying effect that Ga is substituted by Al atoms in the unit cell. Noticeably, κ_l of the sample $x = 0.25$ is much lower than that of the sample Al=4.5, in fact, it is even close to the theoretical minimum lattice thermal conductivity of $Ba_8Ga_{16}Ge_{30}$. The reduction of the κ_l is most likely due to the Al particles, which enhance phonon scattering at mesoscale.

As a result of the improved electron and phonon transport, zT is optimized for the sample $x = 0.25$, with a value of 0.93 at 1073 K (Figure 6.6). Compared to the ternary clathrate $Ba_8Ga_{16}Ge_{30}$ whose maximum zT is 0.67, approximately 50 % enhancement is achieved by microstructure engineering.

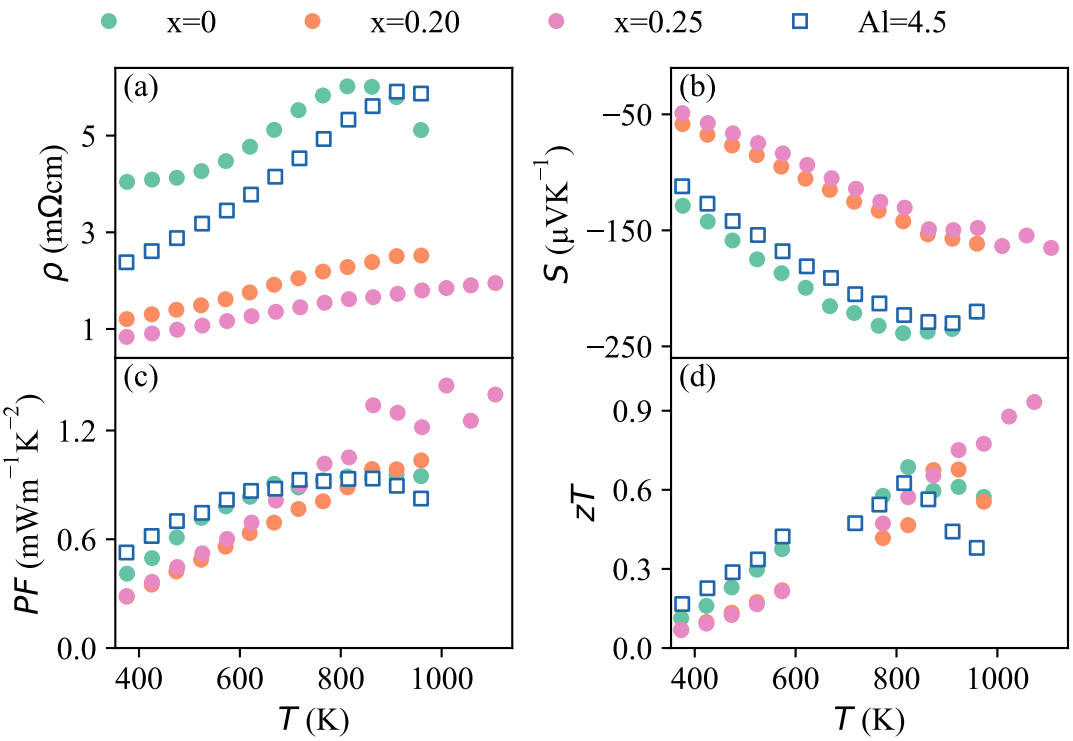

Figure 6.6: *(a) Electrical resistivity, (b) Seebeck coefficient, (c) power factor and (d) figure of merit for* $Ba_8(Al_xGa_{1-x})_{16}Ge_{30}$ *samples,* $x = 0$*, 0.20 and 0.25. Here, sample Al=4.5 is the annealed sample Al=4.5 from* ***Paper IV****.*

7 Conclusion

Inorganic clathrates, as one of the prominent thermoelectric materials, have been studied extensively for decades. Nevertheless, they are questioned sometimes: the materials are seemingly not as thermally stable as thought, and the inconsistency in the thermoelectric properties has not yet been explained. In this thesis, we have tackled two problems regarding the quaternary clathrates $Ba_8Al_xGa_{16-x}Ge_{30}$: the intrinsic order-disorder phase transition, and how to improve the thermoelectric performance.

The order-disorder phase transition in the host structure has been revealed both experimentally and theoretically. The material changes from an ordered ground state to a partially disordered high-temperature configuration, which gives rise to a distinct feature in the specific heat capacity near the transition temperature. The band structure also differs between the ground and the high-temperature states, mainly in the density of states near the Fermi level. Taking the order-disorder transition into account, theoretical calculations have predicted the electrical resistivity and Seebeck coefficient, which is in excellent agreement with the experimental data. Moreover, we have found out that the degree of chemical ordering can be controlled by the synthesis methods, *e.g.*, the flux-grown samples are consistent with the high-temperature disordered configuration, while the Czochralski-grown sample lies between the ground and high-temperature state.

The order-disorder phase transition indicates that the elements are relatively mobile at elevated temperature, if atomic vacancies exist in the host structure, the atomic rearrangement can be quite complex. It is found that for the flux-grown samples $Ba_8Al_xGa_{16-x}Ge_{30}$ with Al content less than 5 atoms per unit cell, atomic vacancies are formed. This further induces a semiconducting-to-metallic transition in the form of a peculiar transition in the electrical resistivity. This peculiar transition was indeed reported previously, however, has not yet been explained. We are able to relate the transition to the atomic vacancies, possibly by the phase transition as the specific heat capacity implies.

Different methods have been employed to improve the thermoelectric performance of quaternary $Ba_8Al_xGa_{16-x}Ge_{30}$ clathrates, *e.g.*, Ce-doping on the guest sites and tuning the carrier concentration. Nevertheless, the most effective way is to engineer the microstructure. More specifically, by alloying 25 % $Ba_8Al_{16}Ge_{30}$ with 75 % $Ba_8Ga_{16}Ge_{30}$, a heterostructure is created which consists of a quaternary clathrate main phase and aggregates of Al particles. Both the electron and phonon transport is improved: the weighted charge carrier mobility of

the sample exceeds that of the single crystal, while the lattice thermal conductivity is close to the theoretical minimum value for the clathrate. As a result, zT is optimized for the $Ba_8(Al_xGa_{1-x})_{16}Ge_{30}$ sample $x = 0.25$, with a maximum value of 0.93 at 1073 K, which is approximately 50 % enhancement compared to the ternary $Ba_8Ga_{16}Ge_{30}$ sample.

In this thesis, a comprehensive understanding of the process-structure-property relationship is achieved for the inorganic clathrates. The methods that we have explored, *e.g.*, controlling the chemical ordering, suppressing the atomic vacancies and engineering the interfaces/microstructure, are applicable for other material systems and can facilitate the future development of thermoelectric materials.

Acknowledgments

The funding from the Swedish Foundation for Strategic Research (SSF) through the Swedish national graduate school in neutron scattering (SwedNess) is gratefully acknowledged.

Thanks to my supervisor, Prof. Anders Palmqvist, for giving me the opportunity of my PhD journey. Thanks for always being open minded, for the useful advice during the discussion, and the attitude towards all the details and the research. It is a great journey throughout my life!

Thanks to my co-supervisor, Prof. Paul Erhart, who has shown me the great passion towards the work and research. Even though we are in different department, I have learned a lot from the way you supervise a PhD student.

Thanks to my examiner Prof. Christian Müller for the very useful advice. Thanks to my Director of graduate studies Prof. Lars Evenäs for being supportive. Great thanks to Nina Kann for all the help. Without you I cannot finish my thesis and defense on time.

Thanks to my collaborators Joakim Brorsson, Ren Qiu, Prof. Paul Erhart, Prof. Takashi Kamiyama, Dr. Takashi Saito and others helping me with the project, without you the work in this thesis could not have been done. We have together created great work and beautiful stories about the thermoelectrics.

Specially thanks to Joakim Brorsson, Andrey Sizov and Samul Fretz, for tutoring me in the beginning of my PhD path.

Thanks to my colleagues in the research group: Andrey, Caroline, Gunnar, Giulio, Joakim, Milene, Ralph, Sam, Sanna and Walter, and all the colleagues in the Applied Chemistry Division. Thank you all for the amazing time.

Finally, thanks to all my friends and my family for everything. Thank my wife Shuxin Zheng for the support, along this long path to the PhD.

References

[1] International Energy Agency `https://https://www.iea.org/`.

[2] Bell, L. E. Cooling, heating, generating power, and recovering waste heat with thermoelectric systems. *Science* **2008**, *321*, 1457–1461.

[3] Snyder, G. J.; Toberer, E. S. Complex thermoelectric materials. *Nature Materials* **2008**, *7*, 105–14.

[4] Pan, Y.; Aydemir, U.; Grovogui, J. A.; Witting, I. T.; Hanus, R.; Xu, Y.; Wu, J.; Wu, C.-F.; Sun, F.-H.; Zhuang, H.-L., et al. Melt-centrifuged $(Bi, Sb)_2Te_3$: engineering microstructure toward high thermoelectric efficiency. *Advanced Materials* **2018**, *30*, 1802016.

[5] Li, J.-F.; Liu, W.-S.; Zhao, L.-D.; Zhou, M. High-performance nanostructured thermoelectric materials. *NPG Asia Materials* **2010**, *2*, 152–158.

[6] Biswas, K.; He, J.; Blum, I. D.; Wu, C.-I.; Hogan, T. P.; Seidman, D. N.; Dravid, V. P.; Kanatzidis, M. G. High-performance bulk thermoelectrics with all-scale hierarchical architectures. *Nature* **2012**, *489*, 414–418.

[7] Zhu, G.; Lee, H; Lan, Y.; Wang, X.; Joshi, G; Wang, D.; Yang, J; Vashaee, D; Guilbert, H; Pillitteri, A, et al. Increased phonon scattering by nanograins and point defects in nanostructured silicon with a low concentration of germanium. *Physical Review Letters* **2009**, *102*, 196803.

[8] Beretta, D.; Neophytou, N.; Hodges, J. M.; Kanatzidis, M. G.; Narducci, D.; Martin-Gonzalez, M.; Beekman, M.; Balke, B.; Cerretti, G.; Tremel, W., et al. Thermoelectrics: From history, a window to the future. *Materials Science and Engineering: R: Reports* **2019**, *138*, 100501.

[9] Voyager - Mission Status `https://voyager.jpl.nasa.gov/mission/status/#sfos`.

[10] He, J.; Tritt, T. M. Advances in thermoelectric materials research: Looking back and moving forward. *Science* **2017**, *357*.

[11] Kauzlarich, S. M.; Brown, S. R.; Snyder, G. J. Zintl phases for thermoelectric devices. *Dalton Transactions* **2007**, 2099–2107.

[12] Christensen, M.; Johnsen, S.; Iversen, B. B. Thermoelectric clathrates of type I. *Dalton Transactions* **2010**, *39*, 978–92.

[13] Takabatake, T.; Suekuni, K.; Nakayama, T.; Kaneshita, E. Phonon-glass electron-crystal thermoelectric clathrates: experiments and theory. *Reviews of Modern Physics* **2014**, *86*, 669.

[14] Dolyniuk, J. A.; Owens-Baird, B.; Wang, J.; Zaikina, J. V.; Kovnir, K. Clathrate thermoelectrics. *Materials Science and Engineering: R: Reports* **2016**, *108*, 1–46.

[15] Rowe, D. M., *CRC HANDBOOK of thermoelectrics*; CRC Press: Boca Raton; New York; London, 1995.

[16] Mao, J.; Liu, Z.; Zhou, J.; Zhu, H.; Zhang, Q.; Chen, G.; Ren, Z. Advances in thermoelectrics. *Advances in Physics* **2018**, *67*, 69–147.

[17] Heremans, J. P.; Jovovic, V.; Toberer, E. S.; Saramat, A.; Kurosaki, K.; Charoenphakdee, A.; Yamanaka, S.; Snyder, G. J. Enhancement of thermoelectric efficiency in PbTe by distortion of the electronic density of states. *Science* **2008**, *321*, 554–557.

[18] Pei, Y. Z.; Shi, X. Y.; LaLonde, A.; Wang, H.; Chen, L. D.; Snyder, G. J. Convergence of electronic bands for high performance bulk thermoelectrics. *Nature* **2011**, *473*, 66–69.

[19] Snyder, G. J.; Snyder, A. H.; Wood, M.; Gurunathan, R.; Snyder, B. H.; Niu, C. Weighted mobility. *Advanced Materials* **2020**, *32*, 2001537.

[20] Qin, F.; Nikolaev, S. A.; Suwardi, A.; Wood, M.; Zhu, Y.; Tan, X.; Aydemir, U.; Ren, Y.; Yan, Q.; Hu, L., et al. Crystal structure and atomic vacancy optimized thermoelectric properties in gadolinium selenides. *Chemistry of Materials* **2020**, *32*, 10130–10139.

[21] Adamczyk, J. M.; Gomes, L. C.; Qu, J.; Rome, G. A.; Baumann, S. M.; Ertekin, E.; Toberer, E. S. Native defect engineering in $CuInTe_2$. *Chemistry of Materials* **2020**.

[22] Shuai, J.; Mao, J.; Song, S.; Zhu, Q.; Sun, J.; Wang, Y.; He, R.; Zhou, J.; Chen, G.; Singh, D. J., et al. Tuning the carrier scattering mechanism to effectively improve the thermoelectric properties. *Energy & Environmental Science* **2017**, *10*, 799–807.

[23] Xie, H. H.; Wang, H.; Fu, C. G.; Liu, Y. T.; Snyder, G. J.; Zhao, X. B.; Zhu, T. J. The intrinsic disorder related alloy scattering in ZrNiSn half-Heusler thermoelectric materials. *Scientific Reports* **2014**, *4*, 6888.

[24] Ma, Y.; Heijl, R.; Palmqvist, A. E. C. Composite thermoelectric materials with embedded nanoparticles. *Journal of Materials Science* **2012**, *48*, 2767–2778.

[25] Zhang, X.; Bu, Z.; Shi, X.; Chen, Z.; Lin, S.; Shan, B.; Wood, M.; Snyder, A. H.; Chen, L.; Snyder, G. J.; Pei, Y. Electronic quality factor for thermoelectrics. *Science Advances* **2020**, *6*.

[26] Koza, M. M.; Johnson, M. R.; Viennois, R.; Mutka, H.; Girard, L.; Ravot, D. Breakdown of phonon glass paradigm in La-and Ce-filled Fe_4Sb_{12} skutterudites. *Nature Materials* **2008**, *7*, 805–810.

[27] Iversen, B. B.; Palmqvist, A. E.; Cox, D. E.; Nolas, G. S.; Stucky, G. D.; Blake, N. P.; Metiu, H. Why are clathrates good candidates for thermoelectric materials? *Journal of Solid State Chemistry* **2000**, *149*, 455–458.

[28] Sales, B. C.; Chakoumakos, B.; Jin, R; Thompson, J.; Mandrus, D Structural, magnetic, thermal, and transport properties of $X_8Ga_{16}Ge_{30}$ (X= Eu, Sr, Ba) single crystals. *Physical Review B* **2001**, *63*, 245113.

[29] Blake, N. P.; Latturner, S.; Bryan, J. D.; Stucky, G. D.; Metiu, H. Band structures and thermoelectric properties of the clathrates $Ba_8Ga_{16}Ge_{30}$, $Sr_8Ga_{16}Ge_{30}$, $Ba_8Ga_{16}Si_{30}$ and $Ba_8In_{16}Sn_{30}$. *The Journal of Chemical Physics* **2001**, *115*, 8060–8073.

[30] Zhao, L.-D.; Lo, S.-H.; Zhang, Y.; Sun, H.; Tan, G.; Uher, C.; Wolverton, C.; Dravid, V. P.; Kanatzidis, M. G. Ultralow thermal conductivity and high thermoelectric figure of merit in SnSe crystals. *Nature* **2014**, *508*, 373–377.

[31] Li, C. W.; Hong, J.; May, A. F.; Bansal, D.; Chi, S.; Hong, T.; Ehlers, G.; Delaire, O Orbitally driven giant phonon anharmonicity in SnSe. *Nature Physics* **2015**, *11*, 1063–1069.

[32] Dong, J.; Sun, F.-H.; Tang, H.; Pei, J.; Zhuang, H.-L.; Hu, H.-H.; Zhang, B.-P.; Pan, Y.; Li, J.-F. Medium-temperature thermoelectric GeTe: vacancy suppression and band structure engineering leading to high performance. *Energy & Environmental Science* **2019**, *12*, 1396–1403.

[33] Zhang, J.; Song, L.; Pedersen, S. H.; Yin, H.; Iversen, B. B., et al. Discovery of high-performance low-cost n-type Mg_3Sb_2-based thermoelectric materials with multi-valley conduction bands. *Nature Communications* **2017**, *8*, 1–8.

[34] Liu, H.; Shi, X.; Xu, F.; Zhang, L.; Zhang, W.; Chen, L.; Li, Q.; Uher, C.; Day, T.; Snyder, G. J. Copper ion liquid-like thermoelectrics. *Nature Materials* **2012**, *11*, 422–425.

[35] Harrison, J.; Hauser, J. Alloy scattering in ternary III-V compounds. *Physical Review B* **1976**, *13*, 5347.

[36] Krishnamurthy, S.; Sher, A; Chen, A.-B. Generalized Brooks' formula and the electron mobility in Si_xGe_{1-x} alloys. *Applied Physics Letters* **1985**, *47*, 160–162.

[37] Yan, X.; Ikeda, M.; Zhang, L.; Bauer, E.; Rogl, P.; Giester, G.; Prokofiev, A.; Paschen, S. Suppression of vacancies boosts thermoelectric performance in type-I clathrates. *Journal of Materials Chemistry A* **2018**, *6*, 1727–1735.

[38] Li, J.; Chen, Z.; Zhang, X.; Yu, H.; Wu, Z.; Xie, H.; Chen, Y.; Pei, Y. Simultaneous optimization of carrier concentration and alloy scattering for ultrahigh performance GeTe thermoelectrics. *Advanced Science* **2017**, *4*, 1700341.

[39] Tamaki, H.; Sato, H. K.; Kanno, T. Isotropic conduction network and defect chemistry in $Mg_{3+\delta}Sb_2$-based layered Zintl compounds with high thermoelectric performance. *Advanced Materials* **2016**, *28*, 10182–10187.

[40] Biswas, K.; He, J.; Zhang, Q.; Wang, G.; Uher, C.; Dravid, V. P.; Kanatzidis, M. G. Strained endotaxial nanostructures with high thermoelectric figure of merit. *Nature Chemistry* **2011**, *3*, 160–166.

[41] Zebarjadi, M.; Joshi, G.; Zhu, G.; Yu, B.; Minnich, A.; Lan, Y.; Wang, X.; Dresselhaus, M.; Ren, Z.; Chen, G. Power factor enhancement by modulation doping in bulk nanocomposites. *Nano Letters* **2011**, *11*, 2225–30.

[42] Kuo, J. J.; Kang, S. D.; Imasato, K.; Tamaki, H.; Ohno, S.; Kanno, T.; Snyder, G. J. Grain boundary dominated charge transport in Mg_3Sb_2-based compounds. *Energy & Environmental Science* **2018**, *11*, 429–434.

[43] Luo, T.; Kuo, J. J.; Griffith, K. J.; Imasato, K.; Cojocaru-Mirédin, O.; Wuttig, M.; Gault, B.; Yu, Y.; Snyder, G. J. Nb-mediated grain growth and grain-boundary engineering in Mg_3Sb_2-based thermoelectric materials. *Advanced Functional Materials* **2021**, 2100258.

[44] Delaire, O.; Ma, J.; Marty, K.; May, A. F.; McGuire, M. A.; Du, M.-H.; Singh, D. J.; Podlesnyak, A; Ehlers, G; Lumsden, M., et al. Giant anharmonic phonon scattering in PbTe. *Nature Materials* **2011**, *10*, 614–619.

[45] Christensen, M.; Abrahamsen, A. B.; Christensen, N. B.; Juranyi, F.; Andersen, N. H.; Lefmann, K.; Andreasson, J.; Bahl, C. R. H.; Iversen, B. B. Avoided crossing of rattler modes in thermoelectric materials. *Nature Materials* **2008**, *7*, 811–815.

[46] Zhou, C.; Lee, Y. K.; Yu, Y.; Byun, S.; Luo, Z.-Z.; Lee, H.; Ge, B.; Lee, Y.-L.; Chen, X.; Lee, J. Y., et al. Polycrystalline SnSe with a thermoelectric figure of merit greater than the single crystal. *Nature Materials* **2021**, 1–7.

[47] Christensen, M.; Lock, N.; Overgaard, J.; Iversen, B. B. Crystal structures of thermoelectric n-and p-type $Ba_8Ga_{16}Ge_{30}$ studied by single crystal, multitemperature, neutron diffraction, conventional X-ray diffraction and resonant synchrotron X-ray diffraction. *Journal of the American Chemical Society* **2006**, *128*, 15657–15665.

[48] Christensen, M.; Iversen, B. B. Host structure engineering in thermoelectric clathrates. *Chemistry of Materials* **2007**, *19*, 4896–4905.

[49] Lindroth, D. O.; Brorsson, J.; Fransson, E.; Eriksson, F.; Palmqvist, A.; Erhart, P. Thermal conductivity in intermetallic clathrates: A first-principles perspective. *Physical Review B* **2019**, *100*.

[50] Shi, X.; Yang, J.; Bai, S. Q.; Yang, J. H.; Wang, H.; Chi, M. F.; Salvador, J. R.; Zhang, W. Q.; Chen, L. D.; Wong-Ng, W. On the design of high-efficiency thermoelectric clathrates through a systematic cross-substitution of framework elements. *Advanced Functional Materials* **2010**, *20*, 755–763.

[51] Schnepf, R. R.; Cordell, J. J.; Tellekamp, M. B.; Melamed, C. L.; Greenaway, A. L.; Mis, A.; Brennecka, G. L.; Christensen, S.; Tucker, G. J.; Toberer, E. S., et al. Utilizing site disorder in the development of new energy-relevant semiconductors. *ACS Energy Letters* **2020**, *5*, 2027–2041.

[52] Ångqvist, M.; Lindroth, D. O.; Erhart, P. Optimization of the thermoelectric power factor: coupling between chemical order and transport properties. *Chemistry of Materials* **2016**, *28*, 6877.

[53] Ångqvist, M.; Erhart, P. Understanding chemical ordering in intermetallic clathrates from atomic scale simulations. *Chemistry of Materials* **2017**, *29*, 7554.

[54] Brorsson, J.; Zhang, Y.; Palmqvist, A. E. C.; Erhart, P. Order-disorder transition in inorganic clathrates controls electrical transport properties. *Chemistry of Materials* **2021**, *33*, 4500–4509.

[55] Cederkrantz, D.; Saramat, A.; Snyder, G. J.; Palmqvist, A. Thermal stability and thermoelectric properties of p-type $Ba_8Ga_{16}Ge_{30}$ clathrates. *Journal of Applied Physics* **2009**, *106*, 074509.

[56] Manière, C.; Durand, L.; Weibel, A.; Estournès, C. Spark-plasma-sintering and finite element method: From the identification of the sintering parameters of a submicronic α-alumina powder to the development of complex shapes. *Acta Materialia* **2016**, *102*, 169–175.

[57] May, A. F.; Toberer, E. S.; Saramat, A.; Snyder, G. J. Characterization and analysis of thermoelectric transport in n-type $Ba_8Ga_{16-x}Ge_{30+x}$. *Physical Review B* **2009**, *80*.

[58] Gustafsson, S. E. Transient plane source techniques for thermal-conductivity and thermal-diffusivity measurements of solid materials. *Review of Scientific Instruments* **1991**, *62*, 797–804.

[59] Saramat, A.; Svensson, G.; Palmqvist, A. E. C.; Stiewe, C.; Mueller, E.; Platzek, D.; Williams, S. G. K.; Rowe, D. M.; Bryan, J. D.; Stucky, G. D. Large thermoelectric figure of merit at high temperature in Czochralski-grown clathrate $Ba_8Ga_{16}Ge_{30}$. *Journal of Applied Physics* **2006**, *99*, 023708.

[60] Puspita, W. R.; Takeya, H.; Mochiku, T.; Ishikawa, Y.; Lee, S.; Torii, S.; Hagihala, M.; Kamiyama, T. In *2019 2nd International Conference on Applied Engineering (ICAE)*, 2019, pp 1–5.